MASTERARBEIT

Titel der Masterarbeit

„Multi-Photon Interference in a Boson Sampling Computation“

Verfasserin

Sarah Stöckl , BA Bakk.

angestrebter akademischer Grad

Master of Science (MSc)

Wien, 2014

Studienkennzahl lt. Studienblatt:	A 066 876
Studienrichtung lt. Studienblatt:	Masterstudium Physik UG2002
Betreuerin / Betreuer:	Assoz. Prof. Dr. Philip Walther

Danksagung

Zu Beginn möchte ich meinem Betreuer Prof. Assoz. Dr. Philip Walther danken, der es mir ermöglicht hat in seiner Forschungsgruppe mitzuarbeiten und im Zuge dessen meine Masterarbeit zu schreiben. Ein großes Danke gebührt auch meinem Kollegen Max Tillmann, der mich unter seine Fittiche genommen hat und von dem ich sehr viel lernen durfte. Mit scheinbar unendlicher Geduld hat er nie eine Möglichkeit ausgelassen mir etwas beizubringen zu wollen.

Vielen Dank an die gesamte Quantengruppe und die besonderen Menschen, mit denen auch außerhalb des Institutes, während gemeinsamen Mittagessen, Kochabenden oder Dachterrassen-Events die Zeit immer sehr lustig war. Ein nicht zu geringer Dank geht auch an Joe Cotter für das Korrekturlesen meiner Arbeit. Durch ihn wurde mein tiroler Englisch für die breite Masse verständlich.

Nicht zu vergessen sind meine besten Freunde Eva, Tina und Samuel. Sie haben mich immer bei allem unterstützt und waren sehr verständnisvoll, wenn mir die Arbeit nicht erlaubt hat so sozial zu sein, wie ich es gerne gewesen wäre.

Zum Schluss möchte ich meiner Mama danken, die mich stets darin bestärkt hat, meine Ziele zu verfolgen. Auch meinem Bruder Lukas gebührt ein großes Danke. Er hat mir immer neuen Mut gegeben, wenn ich einmal vergessen habe, warum ich mich für diesen Weg entschieden habe.

Abstract

Quantum computation has inspired significant interest due to its high potential of outperforming classical computers. However, it is still out of reach to realize a full-scale quantum computer. A good agreement for this problem represent intermediate models of quantum computation, such as boson sampling. Photonic boson sampling processes identical simultaneous photons through a passive linear network to obtain an output distribution relying on non-classical interference. This output probability is proportional to the permanent of the transition matrix, which is hard to compute by conventional computers. In this thesis I will present a review of the intermediate model of quantum computation and in this context describe multi-photon interference. The main part of the thesis is the experimental implementation of a generalized boson sampling computation, which uses the degree of distinguishability to characterize the output distribution with respect to the photons' property. Therefore not just the permanent but also the determinant and all immanents of the transition matrix have to be taken into account. The results of this experiment show a big improvement over earlier performed boson sampling experiments. This method of boson sampling with controllable distinguishability of the involved photons can be applied to all experiments using linear optical networks and single photons.

Zusammenfassung

Quantencomputer sind von großem Interesse, da sie das Potential haben weit mehr zu leisten als klassische Computer. Die Realisierung eines solchen universellen Quantencomputers ist jedoch eine große Herausforderung, da die theoretisch nötigen Bedingungen, mit dem heutigen Stand der Technologie nicht geschaffen werden können. In diesem Zusammenhang bieten sogenannte "Zwischenmodelle" einen guten Kompromiss. Ein solches Konzept ist das sogenannte Boson Sampling, bei dem identische Photonen durch ein passives, lineares Netzwerk geschickt werden um eine Wahrscheinlichkeitsverteilung zu erhalten, die auf nicht-klassischer Interferenz beruht. Diese Verteilung ist proportional zu der Permanenten der komplexen Matrix, die das lineare Netzwerk beschreibt. Da kein effizienter klassischer Algorythmus zur Berechnung einer Matrix mit komplexen Einträgen existiert, bietet die quantenmechanische Version eines Computers die Möglichkeit dieses Problem zu lösen. Der Kern dieser Arbeit ist die Vorstellung eines Experiments, das Boson Sampling einen Schritt weiter führt und anstatt der Permanenten auch die Determinante und Immanenten der Matrix miteinbezieht. Diese Erweiterung ermöglicht eine weit bessere Beschreibung der resultierenden Wahrscheinlichkeitsverteilung und kann dementsprechend für alle Experimente angewendet werden, die auf linearen optischen Netzwerken und einzelnen Photonen beruhen.

Contents

Danksagung i

Abstract iii

Zusammenfassung iv

Preface 1

1 Quantum Information Processing 3
- 1.1 Optical Quantum Computing . . . 3
  - 1.1.1 Photons as qubits . . . 4
  - 1.1.2 Quantum logic gates . . . 7
- 1.2 KLM-Scheme . . . 9
- 1.3 Boson Sampling . . . 11

2 Quantum Interference 17
- 2.1 One Photon Interference . . . 18
- 2.2 Two-Photon Interference . . . 19
  - 2.2.1 Hong-Ou-Mandel Effect . . . 20
  - 2.2.2 Generalized Two-Photon Interference . . . 23
- 2.3 Three-Photon Interference . . . 27

3 Boson Sampling with Controllable Distinguishability 31
- 3.1 Motivation . . . 31
- 3.2 Experimental Implementation . . . 33
  - 3.2.1 Laser System . . . 34
  - 3.2.2 Generating Photons . . . 34
  - 3.2.3 Optical Fibers . . . 38
  - 3.2.4 Linear Optics . . . 40
    - 3.2.4.1 Wave plates . . . 40
    - 3.2.4.2 Beam Splitter . . . 41
  - 3.2.5 Integrated Network . . . 42

3.2.6 Setup 44
3.2.7 State Generation 45
3.2.8 Making measurements 48
3.3 Results 50
3.3.1 Characterization of the Network 50
3.3.2 Coincidence landscapes 55
3.3.3 Comparing data with our theoretical model 60

Conclusion **65**

A Mathmatical Background **67**
A.1 Derivation of the two-photon overlap integral 67
A.2 Three-photon coincident rate 72

B Experimental Data **75**
B.1 Spectral Shape of the Photons 75
B.2 Recorded Data for In124 77
B.3 Data for Plots 78

Bibliography **79**

Curriculum Vitea **84**

Preface

Quantum theory is nowadays one of the most precise theories of nature. The special quantum mechanical effects like entanglement or superposition of states became an essential feature for new insights and technologies. One of the fields, that uses these effects is quantum computing and quantum information processing.

In 1982 the physicist Richard Feynman mentioned the idea that a quantum mechanical system could perform certain computations much more efficiently than a classical computer [1]. Where classical computer bits can only be in a definite state, quantum bits have the ability to be in a superposition of states. Such devices are known as universal quantum computers or quantum Turing machine [2]. The extended Church-Turing thesis [3] claims that all computational problems that are efficiently solvable on realistic physical devices, are more efficiently solvable on a probabilistic Turing machine [4, 5].

Promising candidates for the realization of quantum computers are single photons because they are easy to manipulate and provide a natural robustness against decoherence. However, a full-size realization remains still challenging, because quantum computing is very resource demanding due to the lack of qubit interactions [6, 7]. A first step towards scalable quantum computing was made by Emanuel Knill, Raymond LaFlamme and Gerard Milburn (KLM) in 2001 [8]. They propose in their work a method for quantum computing using only linear optical circuits, single-photon sources, measurement-induced effective non-linearities and single-photon detectors. With this technique successful gate operations and transportation of two-qubit gates into a quantum circuit can be enabled [9, 10], but the required number of indistinguishable ancillary photons for a large scale optical quantum computer appears to be too challenging with current technology.

At this point several intermediate models of quantum computation become interesting [11–13]. Even though these methods can not enable a universal quantum computer they still provide a computational speed-up compared to classical computers. A big benefit of intermediate models is that, in contrast to the KLM scheme, they do not need entangling gate operations, adaptive measurements and ancillary photons. This makes them technically much more feasible. In this thesis the intermediate quantum computation model proposed by Scott Aaronson and Alex Arkhipov [14] is highlighted. They introduce a method to solve sampling problems that are believed to be classically hard by using the photons' mobility and bosonic nature. This model is called boson sampling and shows that interference of single photons in optical networks can connect sampling the bosonic output distribution directly to computing matrix permanents. This problem is seen as classically hard since there exists no efficient classical sampling algorithm for calculating the permanent of a complex entried matrix.

In this thesis I will take a closer look on boson sampling in the context of multiphoton interference. Connecting to that I introduce a generalized experiment on boson sampling, by taking not just the permanent but also the determinant and immanants into account. The superiority of quantum computing over classical computing has already been shown in several experiments, using interfering photons and "Boson Sampling with Controllable Distinguishability" is another one.

Chapter 1

Quantum Information Processing

1.1 Optical Quantum Computing

A quantum computer is a device which uses quantum-mechanical effects to increase computational speed. In a classical computer the basic unit of information is a bit. Bits can only exist in a well defined state, usually “0” or “1”. The basic unit of information in a quantum computer is the so called “qubit” or “quantum-bit”. Qubits possess the property that they can exist in a superposition of states, effectively enabling them to carry more information.

Qubits can be realized in a variety of different physical systems. Linear optical quantum computing (LOQC) represents a particularly convenient method. This is because LOQC requires relatively simple components, namely photons and photon detectors as well as linear optical elements such as beam splitters and phase shifters.

The experiment described later in this thesis performs a quantum computation using photons. In this chapter I will therefore review the theoretical description of photonic qubits before introducing a theoretical scheme for LOQC, namely the Knill-LaFlamme-Milburn (KLM) scheme. I will finish the chapter by presenting an experimental realization of LOQC using boson sampling.

1.1.1 Photons as qubits

A photonic qubit uses the physical state of a photon to carry information. Consider a photon which can be in one of two states $|0\rangle$ and $|1\rangle$, where these states form an orthonormal basis in vector space. In the language of LOQC this can be described by the state vector

$$|\phi\rangle = \alpha|0\rangle + \beta|1\rangle, \tag{1.1}$$

where α and β are the probability amplitudes of finding the photon in the states $|0\rangle$ or $|1\rangle$ respectively, and which satisfy the relation $|\alpha|^2 + |\beta|^2 = 1$. Any quantum mechanical system composed of two distinct states like this can act as qubit.

For scalable quantum computing qubits have to fulfill a few requirements. They are often referred to as "DiVincenzo criteria" [15]. In the following the reasons why photons represent an attractive candidate for qubits are listed:

- **Coupling to the environment should be sufficiently low or at least accurately known.**
  Photons exhibit negligible decoherence because there is minimal interaction with the environment. This enables them to be transmitted over large distances, for example using glass fibers.
- **Generation of many qubits at a time should be feasible.**
  The generation of single photons or entangled photon pairs through spontaneous parametric down-conversion can be an efficient process. This enables many qubits to be generated in quick succession.
- **Initializing, manipulating and reading them out should be possible in a reliable way with high fidelity and low error.** Photons can

be manipulated very easily using simple optical elements. Furthermore, they can be detected with high efficiency using avalanche photo-diodes.

- **Physical system realizing the qubit should be scalable.**
  The optical elements required to manipulate photonic qubits can be miniaturized using micro-fabrication techniques. This enables quantum computation to be performed using compact waveguide chips.

In the experiments presented in this thesis the polarization states of a single photon are used as the basis states for computation. These states are namely the horizontal polarization state vector $|H\rangle$ and the corresponding vertical polarization state vector $|V\rangle$. A convenient illustration of how these basis states can be used for computation is provided by the Bloch sphere, which is shown in figure 1.1. In the Bloch sphere representation of a qubit the surface represents pure states, while mixed states are found within this surface. The poles of the sphere define the state vectors of our system, $|H\rangle$ and $|V\rangle$, and superposition of these states can be described using polar and azimuthal rotations through angles, $\Theta \in [0, \pi]$ and $\varphi \in [0, 2\pi]$. This enables us to rewrite equation (1.1) in the form

$$|\phi\rangle = \cos\left(\frac{\Theta}{2}\right)|0\rangle + e^{i\varphi}\sin\left(\frac{\Theta}{2}\right)|1\rangle. \tag{1.2}$$

In order to know which of the two polarization states our qubit is in, it has to be measured. Measurements destroy quantum mechanical superposition states and as a result are referred to as projective measurements. We can express projective measurements in terms of observables,

$$\mathbf{A} = \sum_m m P_m \tag{1.3}$$

where P_m is the projector of the observable $\mathbf{A}$. Here, the eigenvalues m of the observable $\mathbf{A}$ are the only possible results of this measurement. The probability of getting m after measuring $|\psi\rangle$ is given by

$$p(m) = \langle\psi|P_m|\psi\rangle. \tag{1.4}$$

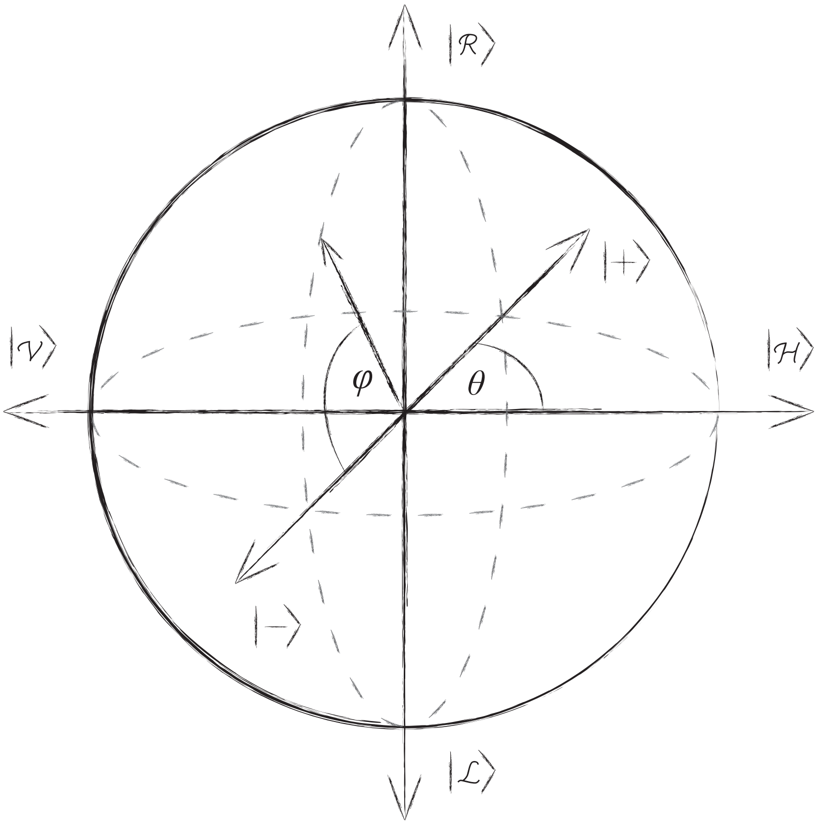

FIGURE 1.1: **The Bloch Sphere.** The Bloch sphere is a well known visualization of a single qubit. A pure state is lying on the surface of the sphere and can be described as a point with the coordinates θ, φ and the radius 1. θ represents an angle on the equatorial plane where $|H\rangle$ and $|V\rangle$ and $|+\rangle$ and $|-\rangle$ are located. The angle φ is measured off the equator and $|R\rangle$ and $|L\rangle$ are placed on the poles of the sphere. All these basis states are separated from each other by $\pi/2$.

Returning now to the Bloch sphere representation of our qubit we can introduce the relevant eigenstates, which are represented by the Pauli spin matrices

$$\sigma_x = \begin{pmatrix} 0 & 1 \\ 1 & 0 \end{pmatrix} ; \sigma_y = \begin{pmatrix} 0 & -i \\ i & 0 \end{pmatrix} ; \sigma_z = \begin{pmatrix} 1 & 0 \\ 0 & -1 \end{pmatrix} . \tag{1.5}$$

where, σ_i represents a rotation around the i^{th} axis and i can take values of x, y and z in the orthogonal Cartesian axes of the Bloch sphere. The polarization states $|H\rangle$ and $|V\rangle$ represent the computational states $|0\rangle$ and $|1\rangle$ and correspond to the poles of the sphere along the z-axes. Due to the orthogonality of the axes, the poles of the x-axes and y-axes represent superpositions of $|H\rangle$ and

$|V\rangle$. These superposition states are written as $1/\sqrt{2}(|H\rangle \pm |V\rangle$, which corresponds to a ±45° linear polarization and has the short form $|+\rangle$ and $|-\rangle$, and as $1/\sqrt{2}(|H\rangle \pm i|V\rangle$, which denotes to right respectively left circular polarized light and has the short cut $|R\rangle$ and $|L\rangle$.

The Pauli matrices are not just essential as eigenstates of the Bloch sphere. They represent three important single-qubit gates, **X**, **Y** and **Z**. In this context, it is useful to give a short overview on quantum gates operating on qubits.

1.1.2 Quantum logic gates

Just as a classical computer relies on logic gates to process information, a quantum computer uses linear transformations as gate operation. The **X** gate for example, causes a bit flip on the input state, like $\alpha|0\rangle + \beta|1\rangle \rightarrow \alpha|1\rangle + \beta|0\rangle$. In quantum computation such a performance is also referred to as a NOT-gate. The **Z** gate just causes a sing change on the input state, like $\alpha|0\rangle + \beta|1\rangle \rightarrow \alpha|0\rangle - \beta|1\rangle$ while the **Y** gate induced a rotation around the y-axes of the Bloch sphere. Another important single-qubit gate is the Hadamard gate. It acts as transformation between the eigenstates of σ_z and σ_x. The corresponding transition matrix is

$$U = \frac{1}{\sqrt{2}} \begin{pmatrix} 1 & 1 \\ 1 & -1 \end{pmatrix} \tag{1.6}$$

and it is essential for quantum computing, because it generates equally weighted superpositions of the computational basis states, like $|H\rangle$ and $|V\rangle$ into $|+\rangle$ and $|-\rangle$. This is why the Hadamard gate is probably the most present gate in quantum algorithms. Quantum gates are represented as unitary matrices and an important feature is that they are reversible. But there are not just single-qubit gates. Using two-qubit gates is essential for quantum computation, because they allow qubits to interact with each other. This means that two-qubit gates can entangle previously independent qubits. One two-qubit gate which is used for such a procedure is the controlled-NOT gate, or CNOT gate

[7], which can be expressed by the unitary matrix

$$\mathrm{CNOT} = \begin{pmatrix} 1 & 0 & 0 & 0 \\ 0 & 1 & 0 & 0 \\ 0 & 0 & 0 & 1 \\ 0 & 0 & 1 & 0 \end{pmatrix}. \tag{1.7}$$

Assuming that a two-qubit state, i.e. $|11\rangle$, is defined by a control qubit at the first entry and a target qubit at the second, the action the gate performs on the qubits can be described as follows. If the control qubit is 0, the target qubit remains unchanged, i.e. $|01\rangle \rightarrow |01\rangle$, but if the control qubit is 1, the target qubit is flipped, i.e. $|11\rangle \rightarrow |10\rangle$. Concerning the ability to create entanglement we can now introduce an intuitive example. Lets assume that our control qubit is in a superposition state $|control\rangle = \frac{1}{\sqrt{2}}(|0\rangle + |1\rangle)$ and the target qubit is $|target\rangle = |0\rangle$. Although these qubits are not entangled, after the CNOT gate, we end up with a maximally entangled Bell-state $|\phi^+\rangle = \frac{1}{\sqrt{2}}(|00\rangle + |11\rangle)$. It is important to mention that in the case of a CNOT gate the operation acts on two qubits in terms of the first one acting as control qubit.

Having now introduced the basic theoretical description of a photonic qubit and some general qubit operations we are ready to describe measurement based quantum computing schemes. There are two prominent proposals for the physical realization of optical quantum computing. These are the one-way quantum computing protocol utilizing cluster states introduced by Raussendorf and Briegel [16] and the KLM architecture by Knill, LaFlamme and Milburn [8]. In the following section I will describe the more general KLM-scheme in detail. I will then describe an experimental intermediate model of quantum computing, namely boson sampling.

1.2 KLM-Scheme

Qubit gate operations are the essential building block for quantum computation. Single-qubit gates require only linear operations for their experimental implementation and are therefore relatively easy to realize. However, the realization of two-qubit gates represents a more significant experimental challenge because it requires the qubits to interact with one another. As mentioned previously photons interact weakly with their environment and even more weakly with one another. Although the non-interacting behavior of photons is beneficial for many aspects of quantum computing experiments, it is a limitation in this particular context.

Early attempts [17] of realizing two-qubit gates used the symmetry properties of bosons and projective measurements. However this technique made clear that optical quantum gates are probabilistic. Regarding a computational circuit there is therefore only a certain success probability $0 < P < 1$ of the post-selection process for each individual gate. This leads to a success probability of P^n for the overall computation based on n gates. This means that simply a computation using CNOT gates would have a success rate of the order of P^{-n}. To overcome this problem it would either be possible to repeat the calculation P^{-n} times or to run it on P^{-n} systems parallel [18]. In both cases the resources scale exponentially with the number of gates.

In 2001 Emanuel Knill, Raymond LaFlamme and Gerard Milburn (KLM) introduced a scheme which enables two-qubit gates to be constructed from single-qubit gates. This, in principle, enables scalable photonic quantum computation using only linear optical circuits, single-photon sources and detectors. Using ancillary photons and adaptive feed-forward techniques the KLM method utilizes the heralding of successful gate operations and furthermore provides a basis for protocols in which probabilistic two-photon gates are teleported into a quantum circuit with high probability. They apply a method in their scheme, Gottesman and Chuang [19] introduced in 1999. The idea is to translate a probabilistic gate action on the output of a quantum computer into a deterministic gate action on auxiliary states. This is an advantage due to the fact that auxiliary states can be duplicated in contrast to the output of a quantum computer. This method is also known as the "teleportation trick", see figure 1.2.

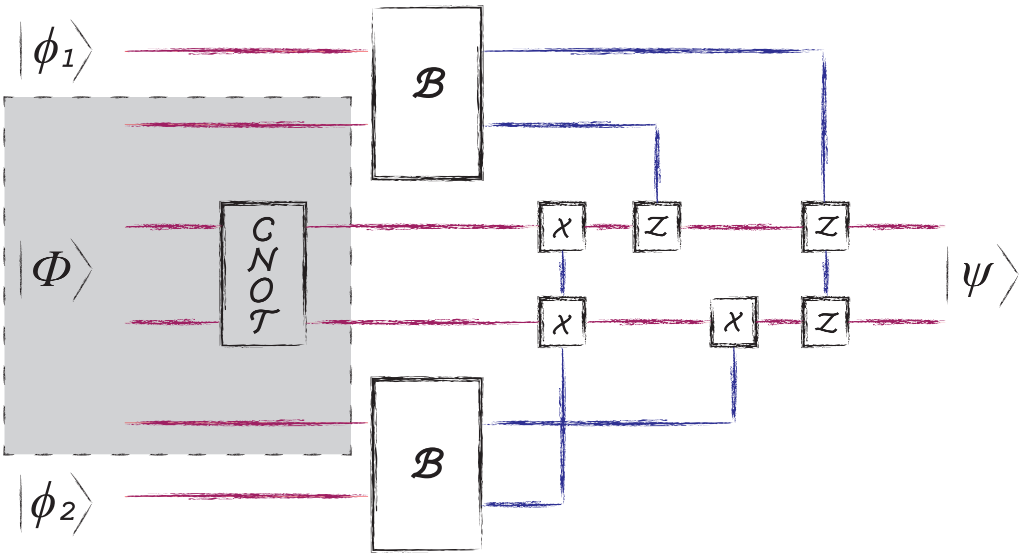

FIGURE 1.2: **The Gottesman-Chuang Gate.** The incoming modes $|\phi_1\rangle$ and $|\phi_2\rangle$ represent the input qubits, to which we want to apply a CNOT operation. They are teleported to the outgoing red modes, which represent the two-qubit gate $|\psi\rangle$. This can be done by using Bell-state measurements (B) and Pauli-operations. The CNOT is performed off-line (shaded box) and the unitaries X, Y and Z compensate for the reordering of the teleportation. The blue lines represent classical communication.

In principle all probabilistic elements in the actual computational circuit can be removed. This can be done by preparing the probabilistic gate offline and it only is teleported into the circuit, whenever it succeeds. By now this sounds quite promising but there is one problem remaining. To outperform this teleportation trick a Bell-state measurement is essential. These measurements are probabilistic as well and can only be performed successfully half of the time. KLM solves this problem by using $2n$ additional photons which results in a success probability of $\frac{n}{n+1}$. As we can see in figure 1.2 a Gottesman-Chuang gate requires two teleportation events, which results in a success probability of $[\frac{n}{n+1}]^2$ for the two-qubit gate. The big problem of this scheme is that it is very resource demanding. 200 ancillary photons are already needed to achieve a

99% success probability of a two-qubit gate. As long as linear optical quantum computing is not scalable due to the resource requirements, it remains more a theoretical approach than a practical implementation for a quantum computer.

In comparison to this theoretical model I introduce a scheme for a practical experimental implementation, which is very resource efficient and also essential for the performed experiment described in this thesis.

1.3 Boson Sampling

A quantum computer can solve mathematically hard problems, which are not solvable using classical techniques. However, a full-scale realization of a quantum computer is out of reach using current technology. One of the main factors presently limiting scalable quantum computing is the requirement for controlled interactions between qubits. In 2011 Aaronson and Arkhipov [14] published a theoretical proposal to realize a quantum system that can outperform a classical computer without the need for logic gates and therefore interactions between qubits. This method represents an intermediate model of a quantum computation referred to as boson sampling, which provides some advantages over a universal quantum computer. Boson sampling is very resource efficient, using only non-interacting bosons and linear-optical networks. There is no need for entangling gate operations, ancillary photons or measurement induced interactions and it is still capable of solving problems which are hard to solve classically. In short, boson sampling provides a method to outperform a classical computer without having to realize a quantum computer.

Boson sampling relies on the random walk process, which can be easily illustrated with a Galton Board as shown in figure 1.3. In the classical case every particle inserted into such a quincunx travels along a channel until it meets an intersection where there is always a 50 : 50 chance that the particle either goes left or right. Assuming that the particles do not interact, then the total probability of finding a particle in a certain output bin is just given by the sum of the independent probabilities for the individual particles.

The quantum version of the Galton board demonstrates significantly different behavior to a classical random walk process, because the particles now demonstrate wavelike properties [20]. These properties of a particle in quantum mechanics are described by their wave function $\Psi(x)$. The wavelike behavior of a particle does not change the fact that the detection refers to a single location in space, however the probability of detection at a certain location is now described through Born's rule [21] as $|\Psi(x)|^2$. Even if the particles do not

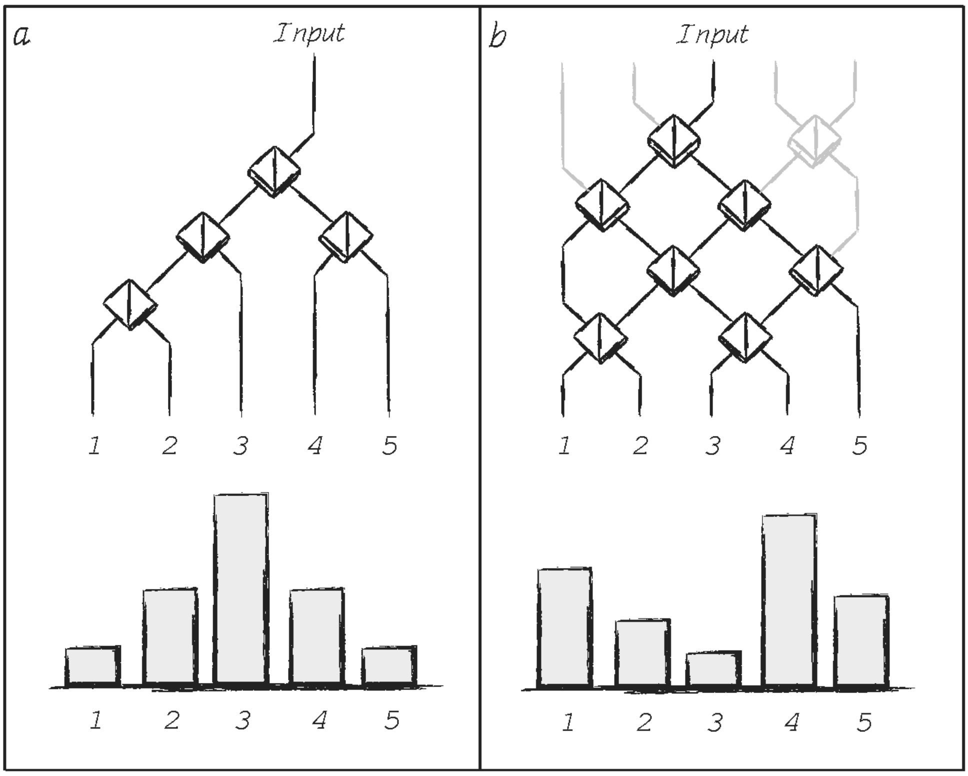

FIGURE 1.3: **The Galton Board.** a) Optical implementation of a classical version of a random walk without biased selection for five output bins. Counting photons at the output samples the binomial distribution. The condition is that there is no interference. This still holds for different photons inserted into multiple inputs. The resulting output distribution would be only a superposition of the individual binomial distributions. b) Quantum random walk implementation for five modes. The only requirement for the splitting ratios of individual elements is that they should be nontrivial. Coupling between modes increases the amount of interference and therefore the complexity of the computation.

physically interact with each other the output probability distribution in the quantum case does not correlate with the individual probabilities of the particles like in the classical case. This is because the combined wavefunction of two indistinguishable particles is symmetric under particle exchange,

$$\Psi(x_1, x_2) = \pm\Psi(x_2, x_1), \tag{1.8}$$

where x_1 and x_2 are the positions of the two particles. The plus sign in this equation refers to bosons, whereas the minus sign refers to fermions. Two identical fermions can never be at the same location since equation (1.8) becomes $\Psi(x_1, x_1) = -\Psi(x_1, x_1)$, which is physically inconsistent. One consequence of equation (1.8) is that bosons tend to bunch while contrastingly fermions anti-bunch. This phenomenon of boson bunching is also known as the "boson birthday paradox" [22].

Regarding the output of such a random walk or Galton board one can sample from the output probability to gain information about it. Four research groups independently implemented a quantum random walk by using indistinguishable bosons (photons) [23–26]. In these experiments photons are guided through a linear optical network which consists of waveguides written into a micro fabricated chip. A schematic illustration of the chip used in the experiment [25] is shown in figure 1.4. Beam splitters on this chip can be realized by writing neighboring channels very close to each other at particular points. There the photons have a certain probability to change the channel. These beam splitters are similar in fashion to modes of the Galton board. Many beam splitters are included on a single chip, which consists of multiple input and output modes. The resulting output probabilities are measured using single-photon detectors. It can be shown that the probability at the output of the interferometric network is proportional to the permanent of the transition matrix, which describes this network [14]. The essence of boson sampling is that by calculating the permanent of an $m \times m$ matrix one is able to determine the probability of any particular output of the network.

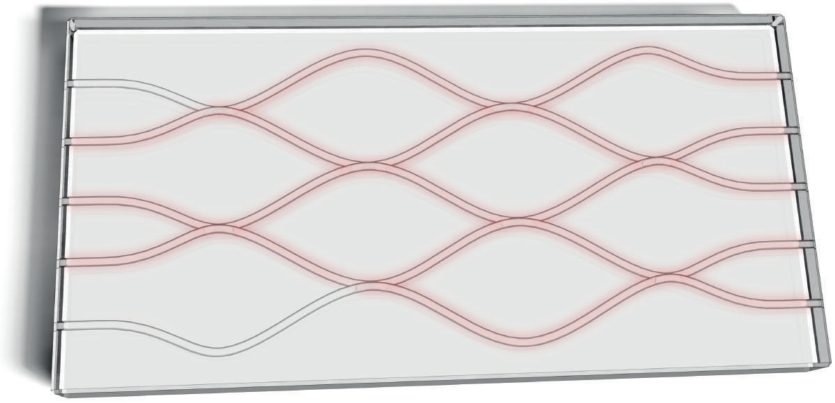

FIGURE 1.4: **Waveguide chip** Illustration of the fabricated chip in the experiment of [25]. Three photons are injected on the left side of the chip. The paths these photons take are illuminated. This picture is the experimental equivalent to the quincunx introduced earlier and shown in figure 1.3.

The permanent of a matrix is the same as the well known determinant except for a minus sign. For example, the permanent of the matrix $A = \left(\begin{smallmatrix} a & b \\ c & d \end{smallmatrix}\right)$ reads $\mathrm{per}(A) = ad + bc$. Many efficient methods exist to calculate the determinant of a matrix on a classical computer. However, the best known classical algorithm for calculating the permanent of a matrix requires an exponentially large number of computational steps and is therefore not feasible for large n, where n is the dimension of the matrix. Let us now try to understand boson sampling computation in more detail [25]. First of all it is necessary to define the permanent of a $m \times m$ matrix A

$$\mathrm{per}(A) = \sum_{\sigma \in S_m} \prod_{i=1}^{m} U_{i,\sigma(i)},$$

where S_m is the set of all permutation of m elements and A is a complex unitary matrix. The computation involves n non-interacting bosons, e.g. photons, operating between m physical modes, e.g. waveguides, where $m > n$. Our input state is defined to be

$$|\phi_{in}\rangle = |i_1, i_2, \ldots, i_m\rangle \tag{1.9}$$

where we assume n bosons occupying m modes, where $i_1 + i_2 + \ldots i_m = n$. For example, the input state $|0, 1, 0, 1, 2\rangle$ represents one boson in the second and forth mode and two in the fifth mode. The probability of finding the output state $|\phi_{out}\rangle = |j_1, j_2, \ldots, j_m\rangle$ is given by

$$P_{\phi_{in},\phi_{out}} = |\langle\phi_{out}|A \otimes A \cdots \otimes A|\phi_{in}\rangle|^2.$$

Scott Aaronson and Alex Arkhipov [14] showed that this probability can be expressed using the permanent,

$$P_{\phi_{in},\phi_{out}} = \frac{|\mathrm{per}(A_{\phi_{in},\phi_{out}})|^2}{i_1!i_2!\ldots i_m!j_1!j_2!\ldots j_m!}.$$

The $n \times n$ matrix $A_{\phi_{in},\phi_{out}}$ can be defined in a very intuitive manner as follows [25]. Consider a 3×3 matrix

$$A = \begin{pmatrix} a & b & c \\ d & e & f \\ g & h & j \end{pmatrix},$$

and the input $|\phi_{in}\rangle = |1, 1, 0\rangle$ and output state $|\phi_{out}\rangle = |0, 1, 1\rangle$. The matrix $A_{\phi_{in}}$ is

$$A_{\phi_{in}} = \begin{pmatrix} a & b \\ d & e \\ g & h \end{pmatrix},$$

and finally $A_{\phi_{in},\phi_{out}}$ reads

$$A_{\phi_{in},\phi_{out}} = \begin{pmatrix} d & e \\ g & h \end{pmatrix}.$$

Applying this example to equation (1.3) the probability for finding a boson in the second and third mode at the output, is given by

$$P_{\phi_{in},\phi_{out}} = |\mathrm{per}(U_{\phi_{in},\phi_{out}})|^2 = |dh - eg|^2.$$

The 3×3 matrix A represents the entire three-moded network. The 2×2 matrix $A_{\phi_{in},\phi_{out}}$ can be constructed from elements of A to form a “submatrix”, where the permanent of this submatrix describes the output probability for the corresponding modes.

The fact that the output probability is proportional to the permanent of a submatrix from the the total transition matrix is crucial for the experiment presented in this thesis. The experiments mentioned in this section focus on just the permanent in relation to boson sampling. Later in this thesis it is shown, that in fact, contributions of the permanent, the determinant and all immanants of the transition matrix have to be taken into account. More about this in chapter 3.

Chapter 2

Quantum Interference

In classical physics interference is the result of a superposition of waves. This implies that the interfering systems have wavelike properties. The most famous experiment showing that light is not just behaving like a particle but also like a wave is the *double-slit experiment* [27–29]. The principle of this experiment is that a coherent light source, such as a laser beam, illuminates a plate. In this plate two parallel slits are cut and behind it there is a screen, where the light pattern can be observed. What can be observed there is an interference pattern consisting of light and dark stripes, as shown in figure 2.1.

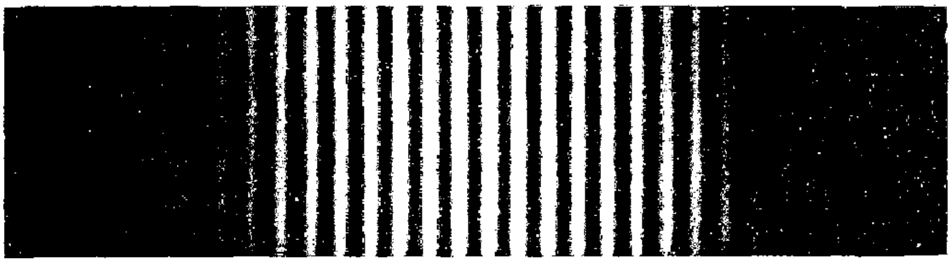

FIGURE 2.1: **Interference pattern.** Figure from http://foundationsofvision.stanford.edu.

This can only be expected if the light exhibits wave nature. However, the detection on the screen shows discrete points which implies that the light consists of individual classical particles. This result demonstrates the principle of wave–particle duality, which is a central concept in quantum mechanics. Therefore lets have a closer look on quantum interference.

2.1 One Photon Interference

In figure 2.2 an optical Mach-Zehnder interferometer is shown. Because of the wavelike nature of light, a photon with wave function A_a is split by the first beam splitter into two partial waves described by the wavefunctions A_1 and A_2. These wavefunctions are recombined at the second beam splitter. The relative phase shift ϕ between A_1 and A_2, in their respective arms of the interferometer, determines the output probabilities for the two output ports of the second beam splitter, where ϕ can be adjusted by varying the position of one of the mirrors. The classical interpretation of this scenario relies on the fact that a photon particle does not split at a beam splitter, but takes one of the two possible ways.

The quantum mechanical interpretation is that one single photon propagates simultaneously in both arms of the Mach-Zehnder as probability amplitudes. The $50:50$ input beam splitter, which can be expressed mathematically by the Hadamard operator

$$U = \frac{1}{\sqrt{2}} \begin{pmatrix} 1 & 1 \\ 1 & -1 \end{pmatrix}, \tag{2.1}$$

creates for every individual photon a superposition of two states, whereas one state represents path 1 and the other state path 2. The input state of the photon can be expressed as $|\phi\rangle = |1\rangle_a|0\rangle_b$ which just means that there is one photon entering the “a” labeled entry of the beam splitter and no photon the “b” labeled one. After transformed by the first beam splitter and gaining a phase shift ϕ in one path the state becomes $|\phi\rangle = \frac{1}{\sqrt{2}}(|1\rangle_1|0\rangle_2 + e^{i\phi}|0\rangle_1|1\rangle_2)$. The final output state of the Mach-Zehnder interferometer we obtain after recombination by the second beam splitter: $|\phi\rangle = \frac{1}{2}(1 + e^{i\phi})|1\rangle_a|0\rangle_b + \frac{1}{2}(1 - e^{i\phi})|0\rangle_a|1\rangle_b$. Therefore the probability of detecting a photon in detector a is $P_a = \frac{1}{2}(1 + \cos\phi)$ and the

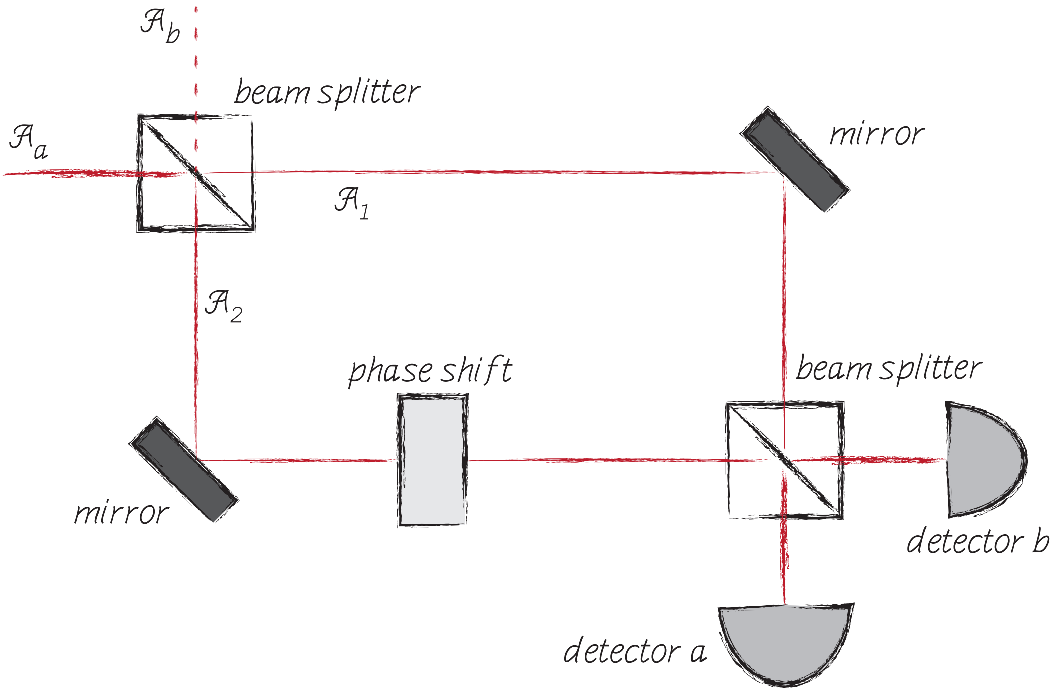
$\mathcal{A}_b$
beam splitter
$\mathcal{A}_a$
mirror
$\mathcal{A}_1$
$\mathcal{A}_2$
phase shift
beam splitter
mirror
detector b
detector a

Figure 2.2: **Illustration of a Mach-Zehnder interferometer.** An incoming wave A_a enters a first 50 : 50 beam splitter and is split into two partial waves A_1 and A_2. The wave taking the lower path gets a phase shift ϕ before the two partial waves are recombined at the second beam splitter. Since the initial wave enters the beam splitter at the "a" labeled entry the input state is $|1\rangle_a|0\rangle_b$.

one of detecting an event in detector b is $P_b = \frac{1}{2}(1 - \cos\phi)$. The fact that it is not clear which path the photon takes, is the origin of quantum interference.

Lets now add a second photon and observe the occurring interference effect.

2.2 Two-Photon Interference

The experiment described in this thesis requires an understanding of multi-photon interference. In the following section I will present the general case of two-photon interference, providing an overview of the various parameters that have to be considered.

2.2.1 Hong-Ou-Mandel Effect

The simplest example of non-classical two-photon interference was first described by Hong, Ou and Mandel [30] in 1987. They performed an experiment, from now on referred to as the HOM experiment, where two indistinguishable photons were sent through the two separate inputs of a 50 : 50 beam splitter and at each output port there was a single-photon detector. What they found was that no coincidence events were ever detected – in other words only one of the detectors ever recorded an event at a time. The reason for this is that the quantum states of the input photons were indistinguishable. As we saw in equation (1.8) the bosonic nature of photons means that their wavefunction is symmetric under particle exchange, which results in bunching. A graphical representation of the HOM experiment and photon bunching at a beam splitter is shown in figure Fig. 2.3.

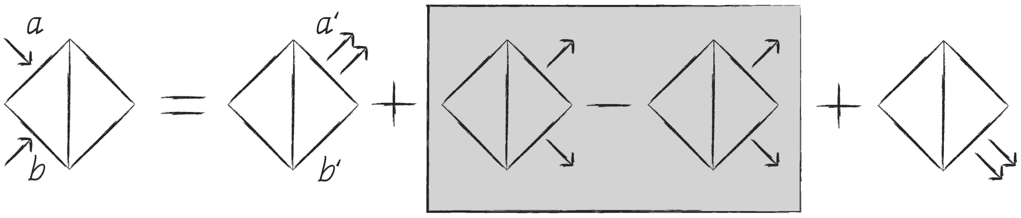

FIGURE 2.3: **Two-photon interference.** When two indistinguishable photons enter a 50/50 beam splitter, the cases where both of them are reflected or transmitted interfere destructively. Therefore the probability of finding the photons in two different output modes is zero. This figure is an intuitive illustration of the bunching behavior of bosons.

The HOM experiment provides a method to quantify the degree of photon indistinguishability and it can be used to characterize the quality of linear optical setups and single-photon sources. Genuine indistinguishability requires temporal and spatial mode-matching of the individual photons. If the photons do not arrive at the beam splitter at the same time their temporal overlap is reduced and so is their indistinguishability. This can be illustrated nicely by varying the arrival times of the photons, using a delay line and recording the coincidence counts at the output port of the beam splitter. What you find is that the coincidence rate increases as the degree of indistinguishability decreases, as shown in figure 2.4. The dip in coincidence counts when the photons are indistinguishable results in the well know Hong-Ou-Mandel dip, or HOM-dip.

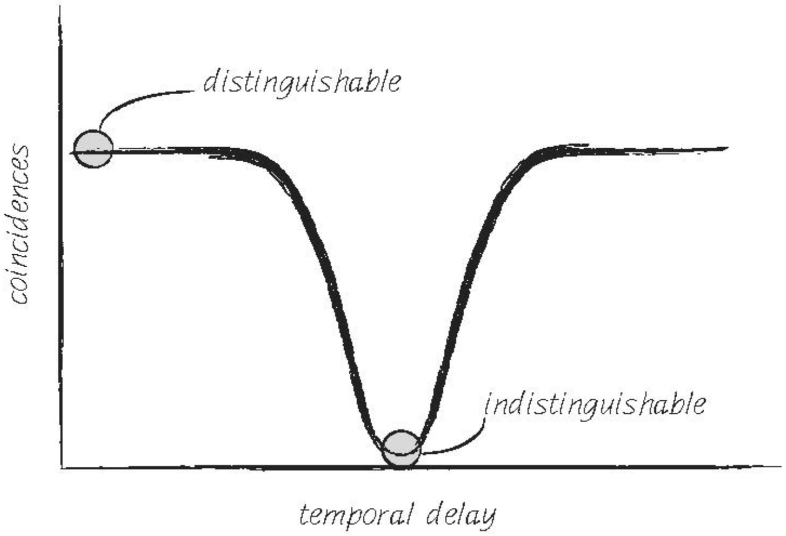

FIGURE 2.4: **Hong-Ou-Mandel dip.** When two photons enter a beam splitter the coincidence rate drops to zero when temporal indistinguishability is achieved. That is referred to the bunching tendency of bosons in quantum mechanics.

Let us now describe the HOM dip mathematically. We can write the input and output states of the system as

$$|\phi_{in}\rangle = \prod_{i=1}^{n} a_i^\dagger |0\rangle \tag{2.2}$$

$$|\phi_{out}\rangle = \prod_{i=1}^{n} \sum_{j=1}^{n} U b_j^\dagger |0\rangle, \tag{2.3}$$

where $|0\rangle$ represents the vacuum state, $a_i^\dagger$ and $b_i^\dagger$ are the creation operators of i photons in the input and output ports respectively and U describes the transition matrix of the beam splitter. We can define U to be

$$U = \begin{pmatrix} \sqrt{\eta} & -i\sqrt{1-\eta} \\ -i\sqrt{1-\eta} & \sqrt{\eta} \end{pmatrix}, \tag{2.4}$$

where η is the reflection coefficient for the field operators. Later it will be important to realize that the bosonic creation operators obey following commutation relations,

$$[a_i, a_j^\dagger] \equiv a_i a_j^\dagger - a_j^\dagger a_i = \delta_{ij} \qquad [a_i^\dagger, a_j^\dagger] = [a_i, a_j] = 0 \qquad \forall\, i, j \tag{2.5}$$

Let us now consider the case where two identical bosons enter different input ports of a $50:50$ beam splitter. For $n = 2$ the transition matrix from equation (2.4) reduces to the Hadamard operator of equation (2.1), which we have already introduced. The corresponding input state from equation (2.2) therefore becomes,

$$|\phi_{in}\rangle = a_1^\dagger a_2^\dagger |0\rangle. \tag{2.6}$$

Using equation (2.3) and the commutator relations (2.5) the output state becomes

$$|\phi_{out}\rangle = \frac{1}{2}[b_1^{\dagger 2} - b_2^{\dagger 2}]|0\rangle, \tag{2.7}$$

which implies that the particles bunch in the same output port. This results in a zero-coincidence rate (see figure 2.4).

We can now connect the output probabilities for the classical and the quantum case with the permanent of the transition matrix, which we introduced in section 1.3. Let us begin by replacing the reflection coefficient in equation (2.4) with $R = \eta$. We can also define the transmission of the beam splitter as $T = 1 - \eta$. The output state is therefore,

$$|\Phi_{out}\rangle = \begin{pmatrix} \sqrt{R} & -i\sqrt{T} \\ -i\sqrt{T} & \sqrt{R} \end{pmatrix} |\Phi_{in}\rangle, \tag{2.8}$$

where $|\Phi_{in}\rangle$ is the input into a network or beam splitter represented by the transition matrix. Assuming that the ansatz $|11\rangle = a_1^\dagger a_2^\dagger|0\rangle$ describes two photons entering two distinct input ports of the beam splitter we get

$$|\Phi_{out}\rangle = -i\sqrt{R}\sqrt{T}(|2\rangle_1|0\rangle_2 + |0\rangle_1|2\rangle_2) + R|1\rangle_1|1\rangle_2 - T|1\rangle_1|1\rangle_2, \tag{2.9}$$

with the subscripts 1,2 labeling the two output ports of the beam splitter. For the case of the $50:50$ beam splitter used in the HOM experiment $R = T = 1/2$. The commutator relation for indistinguishable photons is $[a_1^\dagger, a_2^\dagger] = 0$ which leads to following results for the output states

$$|\langle 1,1||\Phi_{out}\rangle|^2_{\text{indistinguishable}} = |R-T|^2 = 0 \tag{2.10}$$

$$|\langle 1,1||\Phi_{out}\rangle|^2_{\text{distinguishable}} = |R|^2 + |T|^2 = \frac{1}{2} \tag{2.11}$$

If we now use equation (1.3) to calculate the output probability using the permanent of the complex entried $50:50$ beam splitter transition matrix we arrive at the same result, $P_{11} = |Per(U)|^2 = |R-T|^2 = 0$, and we can see that the output probability depends only on the permanent. However, this is only for the case of a perfectly balanced beam splitter using idealized and completely indistinguishable photons. For physically realizable experimental implementations this is not the case and in the following sections I will introduce a method to describe more realistic scenarios.

2.2.2 Generalized Two-Photon Interference

A single-photon state can be described as

$$|1\rangle = \hat{A}^\dagger(\alpha)|0\rangle, \tag{2.12}$$

where the creation operator $\hat{A}^\dagger(\alpha)$ can be written in terms of the excitation integral

$$\hat{A}^\dagger(\alpha) = \int_0^\infty d\omega \alpha(\omega) \hat{a}^\dagger(\omega), \tag{2.13}$$

where $\alpha(\omega)$ is a function that describes the frequency distribution of the excitation and $\hat{a}^\dagger(\omega)$ is the creation operator density in frequency space [31]. The creation and annihilation operators satisfy the commutation relation

$$[\hat{a}_i(\omega), \hat{a}_j^\dagger(\omega')] = \delta_{ij}\delta(\omega - \omega'), \tag{2.14}$$

where the index i is used to label the different photons.

When considering effects involving two photons, $i = 1, 2$, one must include the influence of spectral shape, spatial mode and temporal delay. For our experiments, the spectral function of the photons is well described by the Gaussian function,

$$|\alpha(\omega_i)|^2 = \frac{1}{\sqrt{2\pi}\sigma_i} \exp\left(-\frac{(\omega_i - \Omega_i)^2}{2\sigma_i^2}\right), \tag{2.15}$$

where ω_i is the angular frequency of the i^th photon and Ω_i and σ_i are the mean frequency and standard deviation of the i^th photon distribution respectively. A fit of the spectral shape of the photons used for the experiment is shown in figure 2.5.

If two photons are injected into different input ports of an optical network, built from arbitrary beam splitters and phase shifters, non-classical interference can occur [31]. The generalized input state therefore becomes,

$$|11\rangle = (\hat{A}_1^\dagger(\alpha_1)e^{i\omega_1\tau_1})(\hat{A}_2^\dagger(\alpha_2)e^{i\omega_2\tau_2})|0\rangle, \tag{2.16}$$

where τ_1 and τ_2 are the arrival times of the respective photons. We earlier introduced the concept of symmetry under exchange for indistinguishable bosons. However, in practice this holds only for idealized bosonic particles with perfect temporal overlap, $\Delta\tau = 0$, and no mismatch between their spatial modes.

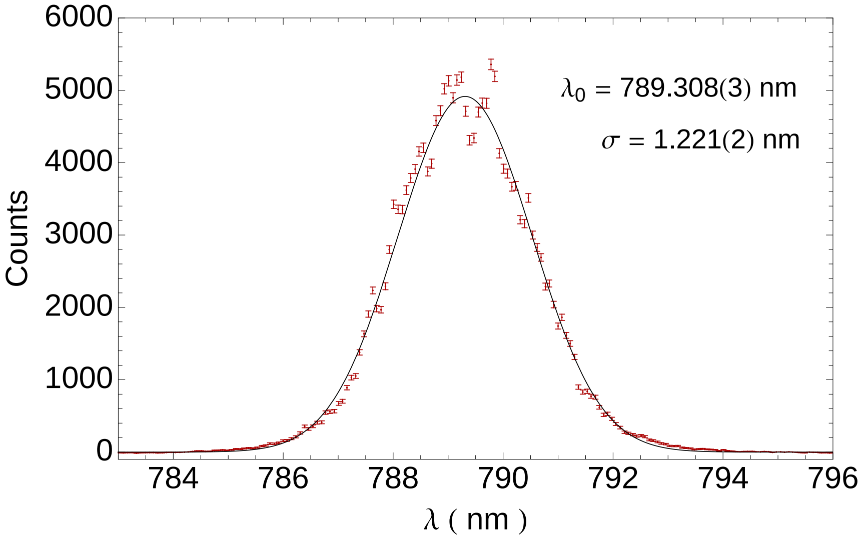

FIGURE 2.5: **Spectral shape**. This Figure shows the spectral shape of one of the three photons used in the experiment.

In order to describe a real experiment using non-idealized photons, it is necessary to define the relative temporal delay, $\Delta\tau = \tau_1 - \tau_2$, between their arrivals. We can calculate the output probability for a network, described by the 2×2 matrix $U = \left(\begin{smallmatrix} U_{11} & U_{12} \\ U_{21} & U_{22} \end{smallmatrix}\right)$ in the conventional manner by tracing over the density matrix describing our system

$$P_{11}(\Delta\tau) = tr(U|11\rangle\langle 11|U^\dagger\, \Pi_1 \otimes \Pi_1), \tag{2.17}$$

where U is operating on the input state $|11\rangle$ and $\Pi_1 = \int d\omega\, a^\dagger(\omega)|0\rangle\langle 0|a(\omega)$ is a positive operator valued measure (POVM) [32]. The POVM describes the measurement outcome of the detectors. This means that for the case of two coincidence photons $|11\rangle$ equation (2.17) can be rewritten in terms of a spectral overlap integral

$$\begin{aligned} P_{11}(\Delta\tau) &= \int d\omega \int d\omega' \langle 11|U^\dagger a_1^\dagger(\omega) a_2^\dagger(\omega')|0\rangle\langle 0|a_1(\omega)a_2(\omega')U|11\rangle \\ &= \int d\omega \int d\omega' \left|\langle 11|U^\dagger a_1^\dagger(\omega) a_2^\dagger(\omega')|0\rangle\right|^2 . \end{aligned} \tag{2.18}$$

As mentioned already, the output probability is proportional to the permanent of the transition matrix only if the involved photons are completely indistinguishable, i.e. $\Omega_1 = \Omega_2$, $\sigma_1 = \sigma_2$ or $\Delta\tau = 0$. As soon as we lose this indistinguishability, $\Omega_1 \neq \Omega_2$, $\sigma_1 \neq \sigma_2$ and $\Delta\tau \neq 0$, the output probability (A.12) becomes proportional to a combination of permanent *and* determinant. We can check this by deriving equation (A.2). Doing so, it is useful to apply the terms

$$\begin{aligned} \mathrm{per}(U) &= U_{11}U_{22} + U_{21}U_{12} \qquad & \mathrm{per}(U) + \det(U) &= 2U_{11}U_{22} \\ \det(U) &= U_{11}U_{22} - U_{21}U_{12} \qquad & \mathrm{per}(U) - \det(U) &= 2U_{21}U_{12}. \end{aligned} \tag{2.19}$$

The result based on permanents and determinants is therefore

$$\begin{aligned} P_{11}(\Delta\tau) = \left(\frac{|\mathrm{per}(U)|^2 + |\det(U)|^2}{2}\right) + \left(\frac{|\mathrm{per}(U)|^2 - |\det(U)|^2}{2}\right) \times \\ \frac{2\sigma_1\sigma_2}{\sigma_1+\sigma_2} \exp\left(-\frac{(\Omega_1-\Omega_2)^2}{2(\sigma_1+\sigma_2)} - 2\Delta\tau^2 \frac{\sigma_1\sigma_2}{\sigma_1+\sigma_2}\right), \end{aligned} \tag{2.20}$$

where we have made the replacements

$$\zeta = \frac{\sigma_1\sigma_2}{\sigma_1^2+\sigma_2^2} \exp\left(-\frac{(\Omega_1-\Omega_2)^2}{2(\sigma_1^2+\sigma_2^2)}\right), \; \xi = \frac{\sigma_1^2\sigma_2^2}{\sigma_1^2+\sigma_2^2}. \tag{2.21}$$

These factors contain all the information, which describe the physical properties of the interfering photons. We therefore obtain the simplified expression

$$P_{11}(\Delta\tau) = \frac{1}{2}\left(|\mathrm{per}(B)|^2 + |\det(B)|^2\right) + \zeta\left(|\mathrm{per}(B)|^2 - |\det(B)|^2\right) \mathrm{e}^{-2\xi\Delta\tau^2}. \tag{2.22}$$

A detailed calculation from (A.2) to (A.12) can be found in the appendix. For perfectly indistinguishable photons equation (A.12) reduces to $P_{11}(0) = |\mathrm{per}(B)|^2$. Genuinely indistinguishable photons are impossible to create – the minimum value in any HOM dip experiment is never zero. In this thesis I will describe what happens when the degree of distinguishability is relatively large by changing the temporal delay between the photon arrivals. Tuning the distinguishability of the interfering photons is equivalent to varying the relative weights of $|\mathrm{per}(U)|^2$ and $|\det(U)|^2$. As soon as more than two photons are involved, this results in relative weightings of the immanants (imm) of the transition matrix [33, 34], of which the permanent and determinant are special cases. The immanent of a matrix is defined as

$$\mathrm{imm}(M) = \sum_{\sigma} \chi(\sigma) \prod_{i} M_{i\sigma(i)} \tag{2.23}$$

for M_{ij} matrix elements of M, where $\chi(\sigma)$ is the character of the permutation σ. For the permanent $\chi(\sigma) = 1$ and for the determinant $\chi(\sigma) = \mathrm{sgn}(\sigma)$. The case with more than two photons and the resulting extension of the formulas introduced previously will be described in the following section.

2.3 Three-Photon Interference

In this section we want to extend the two-photon interference by adding a third photon The theory does not change, but we will see, how the complexity increases by "just" involving another particle. The input state (2.12) for three photons in three distinct spatial modes is expressed by

$$|111\rangle = (A_1^\dagger(\alpha_1) e^{i\omega_1\tau_1})(A_2^\dagger(\alpha_2) e^{i\omega_2\tau_2})(A_3^\dagger(\alpha_3) e^{i\omega_3\tau_3})|0\rangle \ . \tag{2.24}$$

One of the important things we need to consider by adding a third photon is that now two relative delays $\Delta\tau_1 = \tau_1 - \tau_2$ and $\Delta\tau_2 = \tau_3 - \tau_2$ have to be defined. Otherwise the approach is the same as in the two photon case. The input state (2.24) is now transformed by a 3×3 submatrix

$$U = \begin{pmatrix} U_{11} & U_{12} & U_{13} \\ U_{21} & U_{22} & U_{23} \\ U_{31} & U_{32} & U_{33} \end{pmatrix}$$

The transition matrix R transforms the input photons on an output, where the three photons exit in different modes. The output probability or also referred to as coincidence rate, can be written as

$$P_{111}(\Delta\tau_1, \Delta\tau_2) = \int d\omega \int d\omega' \int d\omega'' |\langle 111|U^\dagger a_1^\dagger(\omega) a_2^\dagger(\omega') a_3^\dagger(\omega'')|0\rangle|^2. \tag{2.25}$$

$a_1^\dagger(\omega)$, $a_2^\dagger(\omega')$ and $a_3^\dagger(\omega'')$ stand for creation operators in modes $1, 2,$ and 3 for photons which all have different spectral shape functions dependent on the frequency variables $\omega, \omega', \omega''$. In terms of permanents, determinants and immanants this expression results in a linear superposition of 60 terms [35]:

$$\begin{aligned}
&P_{111}(\Delta\tau_1, \Delta\tau_2) = \int d\omega \int d\omega' \int d\omega'' |\langle 111|\hat{U}^\dagger a_1^\dagger(\omega) a_2^\dagger(\omega') a_3^\dagger(\omega'')|0\rangle|^2 \\
&= \frac{1}{6}|\mathrm{det}(U)|^2 + \frac{2}{9}|\mathrm{imm}(U_{132})|^2 + \frac{1}{9}\mathrm{imm}^*(U_{132})\mathrm{imm}(U_{213}) + \frac{1}{9}\mathrm{imm}(U_{132})\mathrm{imm}^*(U_{213}) \\
&+ \frac{2}{9}|\mathrm{imm}(U_{213})|^2 + \frac{2}{9}|\mathrm{imm}(U_{312})|^2 + \frac{2}{9}|\mathrm{imm}(U)|^2 + \frac{1}{9}\mathrm{imm}(U_{312})\mathrm{imm}^*(U) \\
&+ \frac{1}{6}|\mathrm{per}(U)|^2 + \frac{1}{9}\mathrm{imm}(U)\mathrm{imm}^*(U_{312}) \\
&+ \zeta_{13}\exp(-2\xi_{13}(\Delta\tau_1 - \Delta\tau_2)^2)\Big(- \frac{1}{6}|\mathrm{det}(U)|^2 - \frac{2}{9}\mathrm{imm}(U)\mathrm{imm}^*(U_{132}) - \frac{1}{9}\mathrm{imm}(U)\mathrm{imm}^*(U_{213}) \\
&- \frac{1}{9}\mathrm{imm}^*(U_{132})\mathrm{imm}(U_{312}) + \frac{1}{9}\mathrm{imm}^*(U_{213})\mathrm{imm}(U_{312}) - \frac{1}{9}\mathrm{imm}(U_{132})\mathrm{imm}^*(U_{312}) \\
&+ \frac{1}{9}\mathrm{imm}(U_{213})\mathrm{imm}^*(U_{312}) - \frac{2}{9}\mathrm{imm}(U_{132})\mathrm{imm}^*(U) - \frac{1}{9}\mathrm{imm}(U_{213})\mathrm{imm}^*(U) + \frac{1}{6}|\mathrm{per}(U)|^2\Big) \\
&+ \zeta_{12}\exp(-2\xi_{12}\Delta\tau_1^2)\Big(- \frac{1}{6}|\mathrm{det}(U)|^2 + \frac{1}{9}\mathrm{imm}(U)\mathrm{imm}^*(U_{132}) + \frac{2}{9}\mathrm{imm}(U)\mathrm{imm}^*(U_{213}) \\
&+ \frac{2}{9}\mathrm{imm}^*(U_{132})\mathrm{imm}(U_{312}) + \frac{1}{9}\mathrm{imm}^*(U_{213})\mathrm{imm}(U_{312}) + \frac{2}{9}\mathrm{imm}(U_{132})\mathrm{imm}^*(U_{312}) \\
&+ \frac{1}{9}\mathrm{imm}(U_{213})\mathrm{imm}^*(U_{312}) + \frac{1}{9}\mathrm{imm}(U_{132})\mathrm{imm}^*(U) + \frac{2}{9}\mathrm{imm}(U_{213})\mathrm{imm}^*(U) + \frac{1}{6}|\mathrm{per}(U)|^2\Big) \\
&+ \zeta_{23}\exp(-2\xi_{23}\Delta\tau_2^2)\Big(- \frac{1}{6}|\mathrm{det}(U)|^2 + \frac{1}{9}\mathrm{imm}(U)\mathrm{imm}^*(U_{132}) - \frac{1}{9}\mathrm{imm}(U)\mathrm{imm}^*(U_{213}) \\
&- \frac{1}{9}\mathrm{imm}^*(U_{132})\mathrm{imm}(U_{312}) - \frac{2}{9}\mathrm{imm}^*(U_{213})\mathrm{imm}(U_{312}) - \frac{1}{9}\mathrm{imm}(U_{132})\mathrm{imm}^*(U_{312}) \\
&- \frac{2}{9}\mathrm{imm}(U_{213})\mathrm{imm}^*(U_{312}) + \frac{1}{9}\mathrm{imm}(U_{132})\mathrm{imm}^*(U) - \frac{1}{9}\mathrm{imm}(U_{213})\mathrm{imm}^*(U) + \frac{1}{6}|\mathrm{per}(U)|^2\Big) \\
&+ \zeta_{123}\exp(-I_a + iI_s)\Big(\frac{1}{6}|\mathrm{det}(U)|^2 - \frac{1}{9}|\mathrm{imm}(U_{132})|^2 - \frac{2}{9}\mathrm{imm}^*(U_{132})\mathrm{imm}(U_{213}) \\
&+ \frac{1}{9}\mathrm{imm}(U_{132})\mathrm{imm}^*(U_{213}) - \frac{1}{9}|\mathrm{imm}(U_{213})|^2 + \frac{1}{9}\mathrm{imm}(U)\mathrm{imm}^*(U_{312}) - \frac{1}{9}|\mathrm{imm}(U_{312})|^2 \\
&- \frac{1}{9}|\mathrm{imm}(U)|^2 - \frac{2}{9}\mathrm{imm}(U_{312})\mathrm{imm}^*(U) + \frac{1}{6}|\mathrm{per}(U)|^2\Big) \\
&+ \zeta_{123}\exp(-I_a - iI_s)\Big(\frac{1}{6}|\mathrm{det}(U)|^2 - \frac{1}{9}|\mathrm{imm}(U_{132})|^2 - \frac{2}{9}\mathrm{imm}(U_{132})\mathrm{imm}^*(U_{213}) \\
&+ \frac{1}{9}\mathrm{imm}^*(U_{132})\mathrm{imm}(U_{213}) - \frac{1}{9}|\mathrm{imm}(U_{213})|^2 + \frac{1}{9}\mathrm{imm}^*(U)\mathrm{imm}(U_{312}) - \frac{1}{9}|\mathrm{imm}(U_{312})|^2 \\
&- \frac{1}{9}|\mathrm{imm}(U)|^2 - \frac{2}{9}\mathrm{imm}^*(U_{312})\mathrm{imm}(U) + \frac{1}{6}|\mathrm{per}(U)|^2\Big)\ ,
\end{aligned}$$

with following terms arising from the three-photon spectral overlap integral

$$\begin{aligned}
\zeta_{123} =& \sqrt{\zeta_{12}\zeta_{23}\zeta_{13}}, \\
I_a \equiv& I_a(\Delta\tau_1, \Delta\tau_2) = -(\Delta\tau_1)^2\xi_{12} - (\Delta\tau_1 - \Delta\tau_2)^2\xi_{13} - (\Delta\tau_2)^2\xi_{23}, \\
I_s \equiv& I_s(\Delta\tau_1, \Delta\tau_2) = \Delta\tau_1\nu_{12} + (\Delta\tau_1 - \Delta\tau_2)\nu_{13} - \Delta\tau_2\nu_{23}, \\
\zeta_{ij} =& \frac{2\sigma_i\sigma_j}{\sigma_i^2 + \sigma_j^2} \exp\left(-\frac{(\Omega_i - \Omega_j)^2}{2(\sigma_i^2 + \sigma_j^2)}\right), \\
\xi_{ij} =& \frac{2\sigma_i^2\sigma_j^2}{\sigma_i^2 + \sigma_j^2}, \ \nu_{ij} = \frac{\Omega_i\sigma_j^2 + \Omega_j\sigma_i^2}{\sigma_i^2 + \sigma_j^2}.
\end{aligned} \tag{2.26}$$

This expression is a good example for the occurring difficulty in the three-photon case. Also here the output probability for three indistinguishable photons, i.e.

$$\Omega_1 = \Omega_2 = \Omega_3, \ \sigma_1 = \sigma_2 = \sigma_3 = \sigma, \ \Delta\tau_1 = \Delta\tau_2 = 0, \tag{2.27}$$

reduces from the expression (2.26) to just $P_{111} = |Per(U)|^2$. In [35] The authors show a method to derive from equation (2.26) to a simplified decomposition by introducing six-dimensional vectors and matrices. For basic understanding of multi-photon interference expressed by immanants, it is not necessary to explicate this in the body text, but for the sake of completeness it is shown in the appendix A.

Multi-photon interference is not just a challenge because it is hard to generate a multi-photon input state experimentally. The correct mathematical description requires high precision due to the different physical properties of the involved photons. Since there are no completely indistinguishable photons in real life, to generate a reasonable model describing this effect, one has to take all deviations into account. This is what we did in the experiment boson sampling with controllable distinguishability, which I will now describe in detail in the following chapter.

Chapter 3

Boson Sampling with Controllable Distinguishability

3.1 Motivation

Photonic boson sampling requires non-classical multi-photon interference in an interferometric network. This chapter deals with a version of boson sampling, where the effects of controllable distinguishability are included in order to describe the interfering photons [35]. The motivation for these experiments was to investigate how different sources of error affect a boson sampling computation. In the original proposal of Aaronson and Arkhipov [14] they mention five obvious errors that have to be considered when experimentally implementing a boson sampling computation. These sources of error are,

- photon losses
- imperfect detectors
- inaccurate description of the interferometer
- imperfect preparation of the n-photon Fock-state
- non-simultaneity of photon arrival times

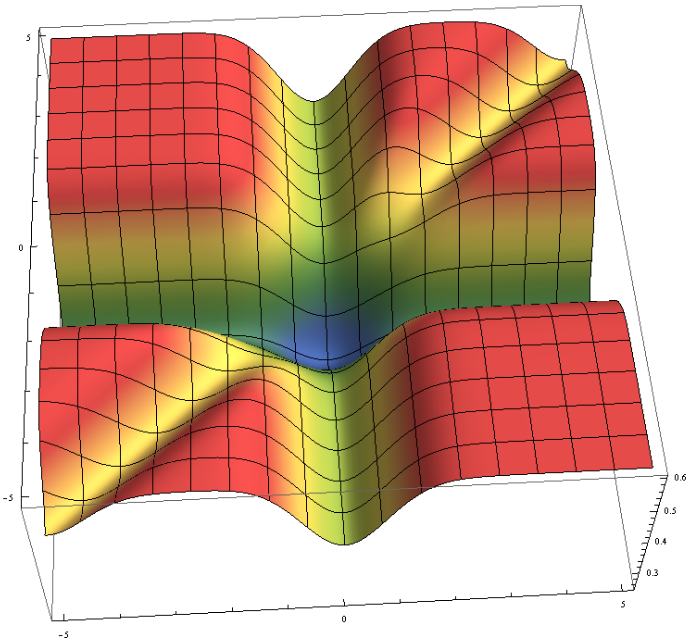

FIGURE 3.1: **Three-photon landscape.** The output probability is shown as a three-dimensional coincidence landscape, where the center shows the quantum case where all three photons are indistinguishable. This point is proportional to just the permanent of the transition matrix, while for every other point on this landscape all immanants of the matrix have to be taken into account.

Photon losses and imperfect detection are two errors which can be corrected quite easily by applying post-selection techniques. I will explain how this is done experimentally later in this thesis. The description of the transition matrix characterizing our interferometer can be improved using stabilization methods and process tomography. A detailed description of this topic is given in the subsection "Characterization of the Network" 3.3.1. Photon-number-resolving detectors with near unit detection efficiency can be used to precisely herald the arrival of incident photons ensuring almost perfect preparation of the n-photon input state [36]. The non-simultaneity of photon arrival times, or more precisely the distinguishability of the photons, used in a boson sampling computation remains the most significant source of error and as such requires significant efforts in order to characterize its influence.

The main goal of this experiment is therefore to investigate the effect of distinguishability in multi-photon interference. Achieving indistinguishable photons is experimentally challenging because there are many parameters which have to be taken into account. Due to a photons nature, a complete indistinguishability needs to cover not just the polarization feature, but also spatial, spectral and temporal properties [37]. All these aspects make multi-photon HOM-dip experiment more hard than expected.

We inject three photons in a five-moded integrated network to measure the multi-photon interference. The variable parameter in the experiment is the relative time delay between the photons, $(\Delta\tau_1, \Delta\tau_2)$. When the time delay between the photons is zero ($\Delta\tau_1 = \Delta\tau_2 = 0$), we measure a three-photon HOM dip. This case has been investigated in the paper "Experimental Boson Sampling" [25].

The coincidence rate, already introduced in the previous section by equation (A.13) can be graphically shown as a three-dimensional coincidence landscape, see figure 3.1 as an example. In the middle of this landscape, where all three photons are indistinguishable, the probability is proportional to the permanent of the transition matrix. By varying the relative time delays, several points on such a landscape can be measured. The different regions of such a landscape are related to different physical behavior of the three photons. Apart from the center, where all photons exhibit maximal indistinguishability, the output probability is not only proportional to the permanent, but as well to determinants and all immanants of the network. These contributions arise from any distinguishability, for example polarization or spectral mode mismatch.

3.2 Experimental Implementation

In this section I will present a detailed review of the apparatus used in the boson sampling with distinguishable photons experiments.

3.2.1 Laser System

The photon source in our experiment is a Titanium Sapphire Laser (Ti:Sapphire) from Coherent, called *Chameleon Ultra II*. The Chameleon is a mode-locked pulsed laser configured for a wavelength range of 680-1080nm. It produces an average infrared power of 3.5 W with a repetition rate of 80 MHz. The Ti-Sapphire oscillator emits 150 fs pulses at a wavelength of 789 nm, which are frequency doubled in a LiB_3O_5 (LBO) crystal through a second harmonic process. The spatial output is in the TEM00 mode and the polarization is horizontal with a purity of 500:1. The output power can be controlled by a power regulation stage consisting of a half-wave plate (HWP) and a polarizing beam splitter (PBS) in front of the LBO-crystal.

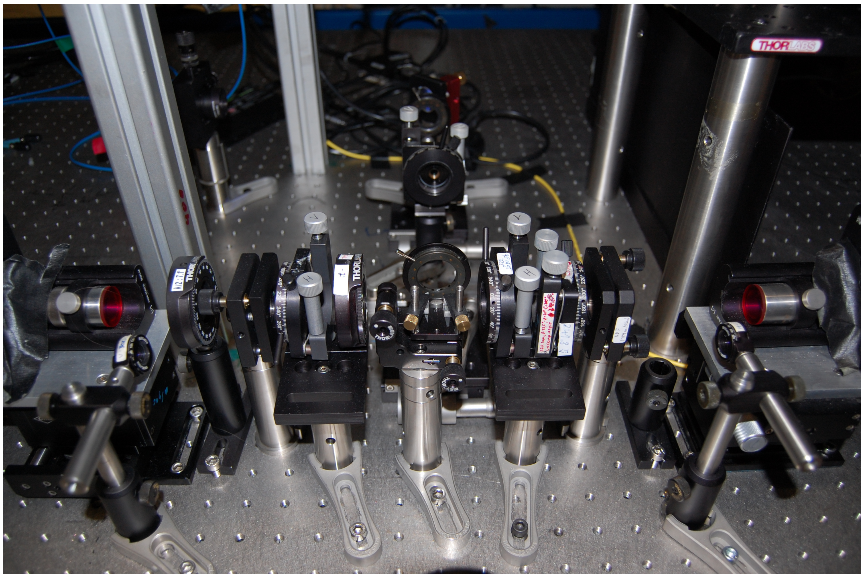

FIGURE 3.2: **SPDC** Picture of the spontaneous parametric down-conversion source in our setup. One can see the pumped BBO crystal, the mirrors and the two couplers with the wave plates and the filters. See also figure 3.12 for intuitive comparison.

3.2.2 Generating Photons

The integration time required to obtain reasonable statistics in experiments using single photons is determined by the rate at which they can be generated.

It is therefore essential to generate them as efficiently as possible. In our experiments we use a process known as spontaneous parametric down-conversion (SPDC) to generate our photon pairs. A picture of our experimental SPDC source is shown in figure 3.2.

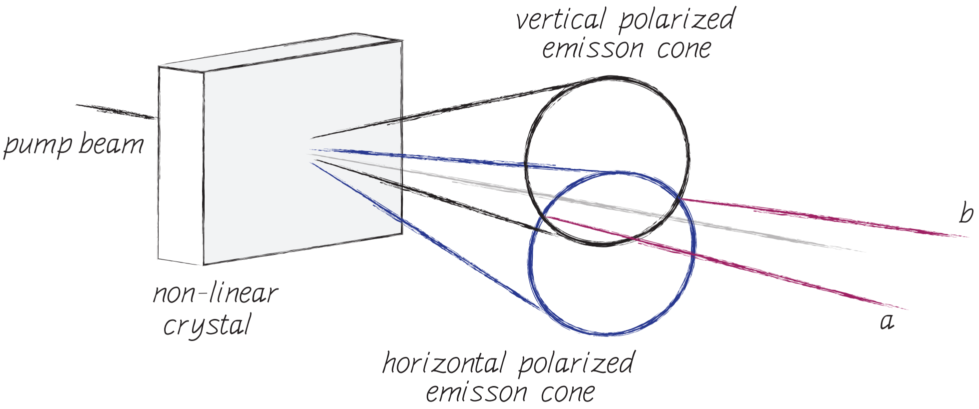

FIGURE 3.3: **Schematic of type-II spontaneous parametric down-conversion.** Inside the non-linear crystal the pump photon splits into two orthogonally polarized emission cones. The horizontal polarized cone is also often referred as "ordinary" polarized and the vertically polarized one as "extraordinary" polarized.

SPDC is a process to produce entangled photon pairs with a high efficiency. The process works by pumping a crystal with a highly non-linear electric susceptibility using light with an energy $\hbar\omega_p$ and a wave vector $\vec{k}_p$. The crystal converts the pump beam into two new beams which in accordance with the laws of conservation for energy and momentum have energies $\hbar\omega_s$ and $\hbar\omega_i$, and momenta $\hbar\vec{k}_s$ and $\hbar\vec{k}_i$, where

$$\omega_p = \omega_s + \omega_i, \tag{3.1}$$

$$\vec{k}_p \approx \vec{k}_s + \vec{k}_i. \tag{3.2}$$

Here I have labeled the indices such that they refer to the "signal" and "idler" beams commonly referred to in quantum optics. Because the photon pairs have different k-vectors they are naturally separated spatially. This makes it easy to collect them.

The orientation of the crystal and the axis along which it is cut determines the phase matching condition. If the two output photons exhibit the same polarization it is referred to as type-I correlation, while if they have perpendicular polarizations it is referred to as type-II, which we use in our setup. The beams emitted by the crystal are rotationally symmetric, leading to two characteristic emission cones referred to as ordinary and extraordinary polarized. This is illustrated in figure 3.3. Due to the birefringence of non-linear crystal the emission cones are non-concentric. At the intersection of the emission cones it is impossible to say which photon belongs to the upper cone and which to the lower cone. At these points, labeled a and b in figure 3.3, the photons are polarization entangled.

Due to group velocity mismatch inside the birefringent crystal, the two photons show a different propagation behavior. This resulting distinguishability has to be compensated to render them entangled. This can be done experimentally with compensation crystals which are from the same type as the birefringent crystal in the down-conversion source and additional half-wave plates. The only difference is that for the compensation the crystals have to be of half the thickness, shown in figure 3.4.

If this is done well, temporal and spatial walk-off effects can be canceled and the entangled state emitted by the source is

$$|\psi\rangle = \frac{1}{\sqrt{2}}(|H\rangle_a|V\rangle_b + e^{i\varphi}|V\rangle_a|H\rangle_b) \tag{3.3}$$

H and V denote to horizontal and vertical polarization and the phase φ arises from the crystal birefringence. The value of this parameter can be changed as desired by using additional birefringent elements or even by tilting the compensation crystal. Additionally to this wave plates can be used to rotate the polarization of the beams. With such a compensation scheme any of the four

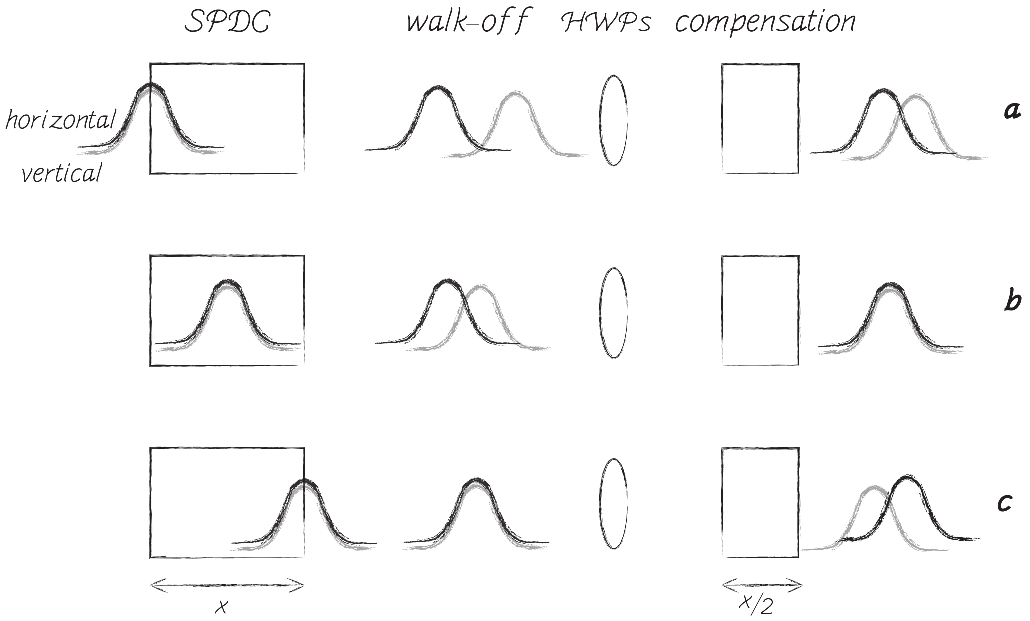

Figure 3.4: **Compensation scheme for temporal walk-off. a)** The photon pair is produced at the beginning of the crystal which gives the vertical polarized wave the maximal phase shift φ. After the polarization switching half-wave plate (HWP) the compensation crystal gives the vertical polarized wave, which is now behind, only a phase shift of $\varphi/2$. This is too less to overlap the waves again. **b)** The two waves have a $\varphi/2$ introduced walk-off which can be compensated by the second crystal. **c)** The waves have no walk-off, because they are produced at the end of the crystal. That leads to an introduced walk-off after the compensation crystal.

Bell states can be produced,

$$|\psi^{\pm}\rangle = \frac{1}{\sqrt{2}}(|H\rangle_a|V\rangle_b \pm |V\rangle_a|H\rangle_b) \tag{3.4}$$

$$|\phi^{\pm}\rangle = \frac{1}{\sqrt{2}}(|H\rangle_a|H\rangle_b \pm |V\rangle_a|V\rangle_b). \tag{3.5}$$

The two orthogonally polarized wave packets have different group velocities which leads to a certain time difference between them, depending on where inside the crystal they are produced. The compensation scheme in figure 3.4 shows different scenarios of this case. After the crystal the two waves have a certain walk-off but the compensation crystal introduces half of the phase shift, which could maximally occur in the first crystal. The half wave plates in the scheme switches the polarization of the incoming waves to ensure a phase difference of zero. For visual explanation of this problem please see figure 3.4.

The SPDC source in our experiment is aligned to emit a four-photon state, which can be expressed as

$$|\psi\rangle = \frac{1}{\sqrt{3}}(|HH\rangle_a|VV\rangle_b + |VV\rangle_a|HH\rangle_b + |HV\rangle_a|HV\rangle_b). \tag{3.6}$$

3.2.3 Optical Fibers

Optical fibers are essential for our experiments. In order to know the difference between the various types of fibers, I will describe them in more detail [38]. An optical fiber is made of low-loss material and acts as a dielectric waveguide with cylindrical shape. The central core of the fiber is surrounded by a cladding layer with a lower refractive index which results in light being guided by the core. Light propagating inside a fiber can only do so by populating particular transverse electromagnetic modes (TEM). If the diameter of the core is so small that only one mode is supported, the optical fiber is described as SINGLE-MODE (SM). Alternatively, optical fibers with large core diameters, which can support

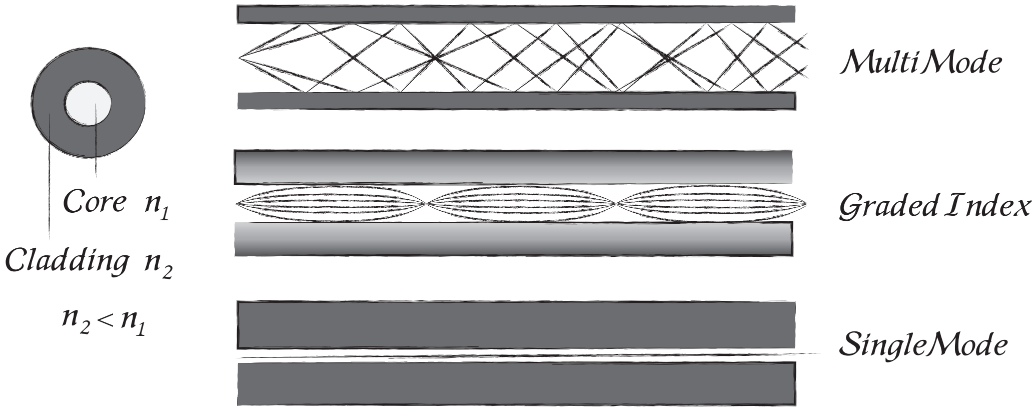

FIGURE 3.5: **Fibertypes.** The three different types of fiber introduced in the text. Coupling into a MM fiber is relatively easy whereas coupling into SM fiber is more challenging due to the much smaller diameter of the core. A good compromise is provided by GRIN fibers which collect more than just one mode, but focuses the modes inside the fiber to achieve a reasonable output signal.

many modes simultaneously are called MULTI-MODE FIBERS (MM). Coupling light into a MM-fiber is significantly easier than into a SM-fiber, because they have a much larger numerical aperture. However, there is a significant disadvantage relating to light propagation in MM-fibers. Because the individual modes propagate with different group velocities, which results in a broadening of the light pulse, the different modes take different times to travel a fixed distance. This subsequently reduces the temporal overlap between pulse signals. This effect, known as modal dispersion, is most dominant in step-index MM-fibers and can be reduced significantly by using graded-index MM-fibers (GRIN MM). Conventional step-index fibers have a constant refractive index in their core and cladding, whereas the refractive index of graded-index fibers is graduated from a maximum value at the center to the minimum at the core-cladding boundary [38]. An illustration of different fiber types is shown in figure 3.5.

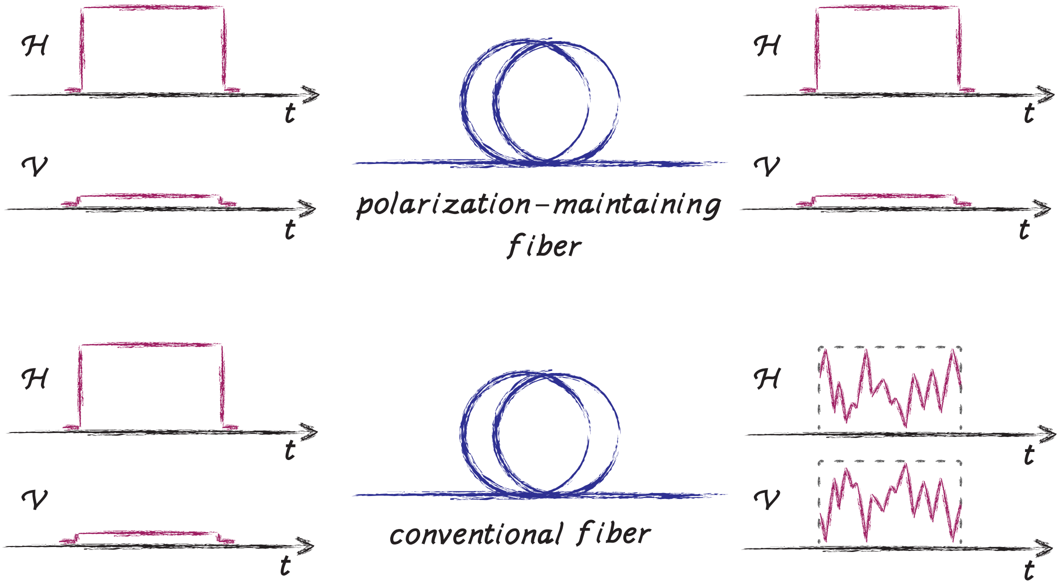

FIGURE 3.6: **PM fiber vs. conventional fiber.** In the upper case a photon with polarization $|H\rangle$ is transmitted through a polarization maintaining fiber. The polarization on the output is still $|H\rangle$, whereas in the lower case the polarization becomes mixed and the photon on the output exhibits no pure $|H\rangle$ polarization anymore but rather a superposition of $|H\rangle$ and $|V\rangle$. Figure adapted from [38]

Another kind of fiber and specially important for our experiment is the POLARIZATION MAINTAINING FIBER[38]. These fibers are single mode fibers but the fundamental difference is that light maintains its linear polarization during propagation through the fiber. Using such fibers is mandatory for experiments where preserving polarization is essential, like in our case. The two orthogonal polarizations propagating through a conventional single-mode fiber, have the same group velocity and there should be no power exchange between the polarization components. However, slightly bending the fiber or random appearing birefringence in the fiber leads to a power transfer. The result of this is that on the output of the fiber the polarization is randomly rotated, see figure 3.6.

3.2.4 Linear Optics

The manipulation of quantum states is essential for quantum information processing. As already mentioned, photonic qubits have the advantage of being manipulated very efficiently using linear optical devices. In our experiments we use an integrated circuit and bulk optics, such as mirrors, wave plates and beam splitters, to perform operations. Some of these elements are described in more detail below.

3.2.4.1 Wave plates

Wave plates are birefringent crystals which introduce a polarization dependent phase shift. Although in principle any retardation phase angle is possible in practice, half-wave plates (HWP) and quarter-wave plates (QWP) are the most commonly used. The half-wave plate rotates the polarization axis of linearly polarized light, whereas the quarter-wave plate converts linearly polarized light into elliptically polarized light, where circularly polarized light is a special case. Using wave plates makes it possible to introduce a controlled phase shift between the two polarization components of the wave passing through. When the optical axis is parallel to the front face of the crystal with thickness d, the relative phase difference between the ordinary and extraordinary beam is given by

$$\Delta\varphi = \frac{2\pi}{\lambda} d|n_o - n_e| \tag{3.7}$$

where n_o and n_e denote the refractive index of the respective beams. This relative phase shift results in $\Delta\varphi = \pi$ for the half-wave plate and $\Delta\varphi = \pi/2$ for the quarter-wave plate.

Let us recall the Bloch sphere. Here the phase shifts correspond to rotations of the polarization vector on the surface of the sphere. If we introduce the angle Θ of the optical axis in the two-dimensional space. Subsequently, the actions of the two different wave plate types can be written as unitary matrices [38, 39]:

$$U_{HWP}(\Theta) = e^{i\pi/2} \begin{pmatrix} \cos 2\Theta & \sin 2\Theta \\ \sin 2\Theta & -\cos 2\Theta \end{pmatrix} \tag{3.8}$$

$$U_{QWP}(\Theta) = \frac{1}{\sqrt{2}} \begin{pmatrix} 1 + i\cos 2\Theta & i\sin 2\Theta \\ i\sin 2\Theta & 1 - i\cos 2\Theta \end{pmatrix} \tag{3.9}$$

By using wave plates any unitary transformation in qubit space can be realized. In our experimental setup these optical elements are very important – because the experiment relies on indistinguishable photons we require all photons to have the same polarization.

3.2.4.2 Beam Splitter

Beam splitters (BS) are one of the basic tools in optical quantum information processing. They reflect a fraction of the incoming intensity (η) and transmit the remaining part $(1 - \eta)$. For a 50/50 beam splitter $\eta = 1/2$. If η is polarization dependent, the optical device can be used to distinguish different polarizations of the incoming light. We then refer to these as polarizing beam splitter (PBS). A PBS usually transmits horizontally polarized light and reflects vertically polarized light, $\eta_H = 0, \eta_V = 1$.

In order to generate a coincidence, which means two counting events at both outputs of the beam splitter, two orthogonally polarized photons have to enter the PBS in the same input port.

If two orthogonally polarized photons enter the same input port of a PBS a single phonon can be counted coincidentally at the two output ports. If both detectors click we refer to this as a coincidence count. Such coincidence counting methods are essential to boson sampling and will be discussed in more detail later.

3.2.5 Integrated Network

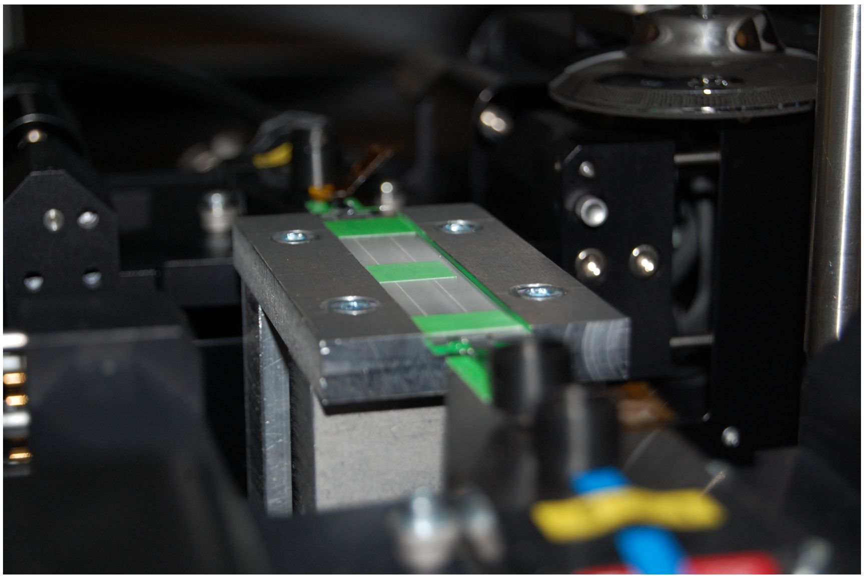

Figure 3.7: **Close-up view of our chip.** The chip is 10 cm long and 2 cm wide. It is hold by an aluminum mount.

Optics experiments rely on light being transmitted from one location to another. Depending on the experiment the distances between locations can vary significantly. Under realistic experimental conditions the light which is traveling in free space, diffracts and broadens as it propagates, due to imperfections in the apparatus. These effects can be compensated by using refocusing lenses and mirrors, but bulk optics are large and is possible that they scatter or even block the light beams. It is therefore useful to apply guided-wave optics [38] similar to optical fibers.

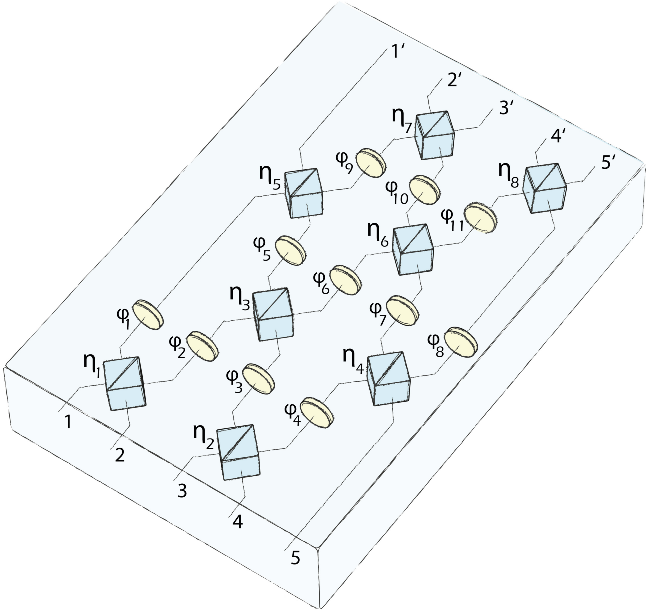

FIGURE 3.8: **Integrated photonic network.** Schematic drawing of the optical network. The circuit consists of eight directional couplers ($\eta_1 ... \eta_8$), eleven phase shifters ($\phi_1 ... \phi_{11}$), five input modes (1...5) as well as of five output modes(1'...5'). To allow coupling to the waveguide with standard fiber-arrays the input and output modes are separated 127 µm and the total length of the chip is 10 cm.

In our experiment we use an integrated waveguide chip, which consists of eight beam splitters and eleven phase shifts. The chip is 10 cm long and shown in figure 3.8. It is very compact in comparison to the same amount of optical components in form of bulk optics. In addition to this network there are two further circuits and a few directional couplers written into the chip. The chip is fabricated by collaborating physicists of the University of Jena in Germany. They use a femto-second direct-writing technology [40], where laser pulses are focused 370 µm below the surface of a high-purity fused silica wafer by an NA = 0.6 objective. The 200 nJ pulses have a pulse duration of 150 fs at 100 kHz repetition rate and a wavelength of 800 nm. The wafer was translated with a speed of 6 cm/s to write the individual waveguides. A schematic illustration of the writing setup is shown in figure 3.9. The modes of these waveguides exhibit a mode field diameter of 21.4 µm × 17.2 µm for a wavelength of 789 nm. The propagation loss is 0.3 dB/cm when combined with the inherent coupling loss of the system we achieve a total waveguide loss of −3.5 dB using PM fibers.

Since MM fibers are used at the output of the integrated circuit the loss there is negligible.

A picture of the waveguide that was used in our setup is shown in figure 3.7.

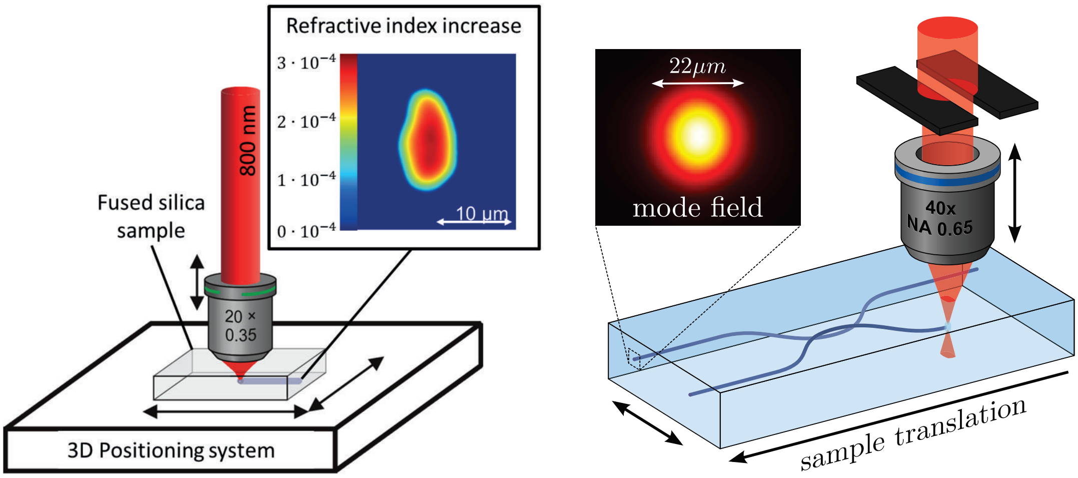
Refractive index increase
$3 \cdot 10^{-4}$
$2 \cdot 10^{-4}$
$1 \cdot 10^{-4}$
$0 \cdot 10^{-4}$
10 μm
800 nm
Fused silica sample
20 ×
0.35
3D Positioning system
22μm
mode field
40x
NA 0.65
sample translation

FIGURE 3.9: **Writing Setup.** On the left side the writing setup is shown, where femto-second laser pulses are focused into a bulk material to create a refractive index change. The sample is translated by a high precision positioning system. The illustration on the right side shows the three-dimensional writing process. Writing with a NA = 0.65 objective results in nearly circular symmetric mode fields with a diameter of $\approx 2.2\mu m$. Figure from [25].

3.2.6 Setup

Two pairs of photons are generated using spontaneous parametric down-conversion (SPDC). These are then distributed into four spatial modes using two PBSs. Three of these four modes are coupled to the integrated circuit, while the fourth one leads directly to a detector used for triggering. To achieve the desired input state we post-select only four-fold coincidence events, namely three separate detection events on the output of the network and one event at the trigger detector. The length of the fibers connected to the input of the chip can be varied using delay lines. This allows us to tune the distinguishability of the photons injected into the network. Figure 3.10 illustrates our setup, consisting of an integrated circuit using eight beam splitters, eleven phase shifters.

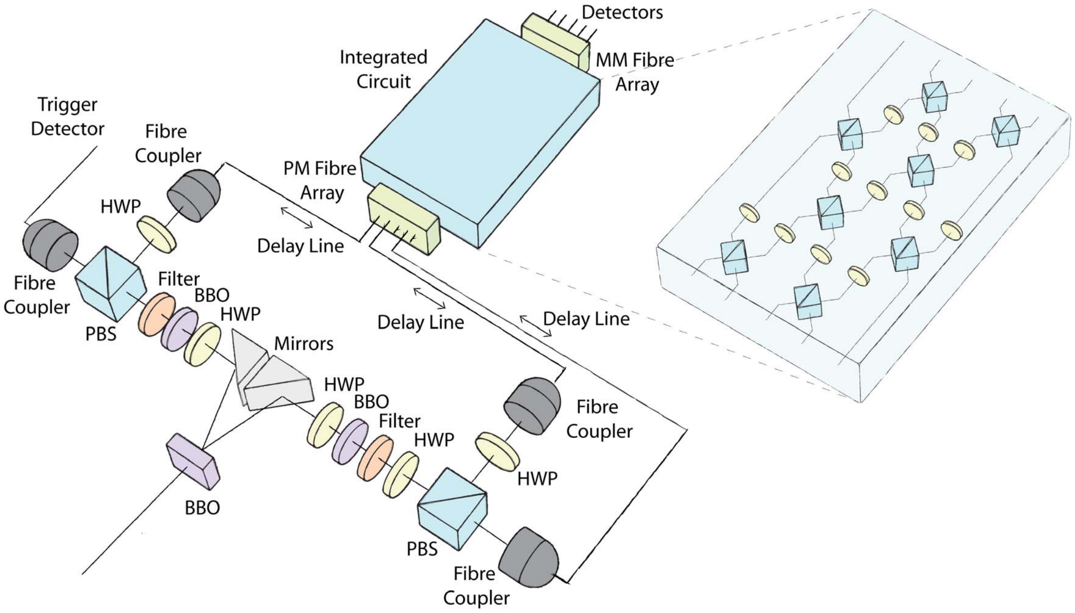
Detectors
Integrated Circuit
MM Fibre Array
Trigger Detector
Fibre Coupler
PM Fibre Array
HWP
Delay Line
Fibre Coupler
Filter
BBO
HWP
PBS
Mirrors
Delay Line
Delay Line
HWP
BBO
Filter
HWP
Fibre Coupler
HWP
BBO
PBS
Fibre Coupler

Figure 3.10: **Experimental Setup of Boson Sampling with controllable distinguishability.** The source emits two photon pairs which are rendered to indistinguishability with wave plates, filters and BBOs. After split into four single photons three of them are directly guided to the waveguide. Delay lines are used to vary the length of the modes and therefore the distinguishability of the photons. The integrated circuit consists of eight beam splitters and eleven phase shifters and is shown in a Mach-Zehnder decomposition.

3.2.7 State Generation

The pump beam has a wavelength of 394.5 nm and is focused on a 2 mm thick β-BaB$_2$O$_4$ (BBO) crystal cut for degenerate non-collinear type-II down-conversion. To reduce temporal and spatial walk-off a compensation scheme consisting of HWPs and 1 mm thick BBO-crystals is applied. The two outputs of the down-conversion source are guided through narrow band interference filters with λ_{FWHM} =3 nm. This is used to render the photons close to spectral indistinguishability and to achieve a coherence time greater than the birefringent walk-off, which is caused by group velocity mismatch in the crystal ($|v_{g_e} - v_{g_o}|$ × half crystal thickness). The down-conversion-source is aligned to emit the maximally entangled Bell-state

$$|\phi^+\rangle = \frac{1}{\sqrt{2}} \left(|H\rangle_a|H\rangle_b + |V\rangle_a|V\rangle_b\right), \tag{3.10}$$

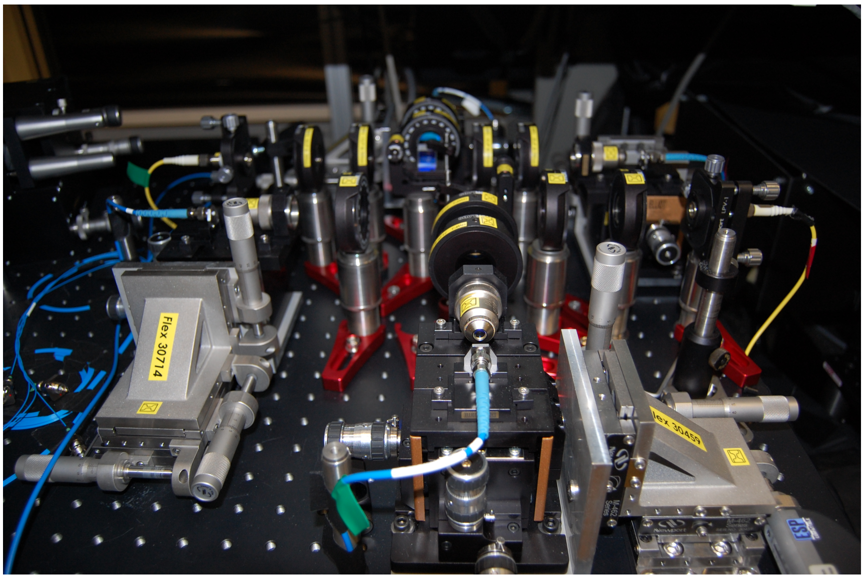

Figure 3.11: **State preparation Stage.** Total view of the state preparation stage consisting of the two outputs of the source, the two polarizing beam splitter cubes and the four spatial modes. The couplers are fixed on translation stages, which can be translated via motorized screws.

when pumped at 205 mW cw-equivalent pump power. $|H\rangle$ denotes to horizontal and $|V\rangle$ to vertical polarization, whereas a and b are the two emission-modes. For our experiment we need a four-photon emission. This can be achieved by setting the pump power to 700 mW. The emitted state we get is

$$|\psi\rangle_{a,b} = \frac{1}{\sqrt{3}}(|HH\rangle_a|HH\rangle_b + |HV\rangle_a|HV\rangle_b + |VV\rangle_a|VV\rangle_b). \tag{3.11}$$

This state is coupled into single-mode fibers equipped with pedal-based polarization controllers to counter any stress-induced rotation of the polarization inside the fiber. Each of these spatial modes a and b is then focused on a polarizing beam splitter cube (PBS). The outputs of the PBSs pass HWPs to ensure that all photons exhibit the same polarization before they are coupled into four PM fibers. Via motorized screws on the couplers, a temporal delay between the photons can be introduced.

The PM fibers are mated to a SM fiber v-groove-array and coupled to the waveguide chip. The output fiber array consists of a MM fiber v-groove-array to collect as many photons as possible. The photons then are detected by single-photon avalanche photo diodes and recorded by a Field Programmable Gate Array (FPGA) logic.

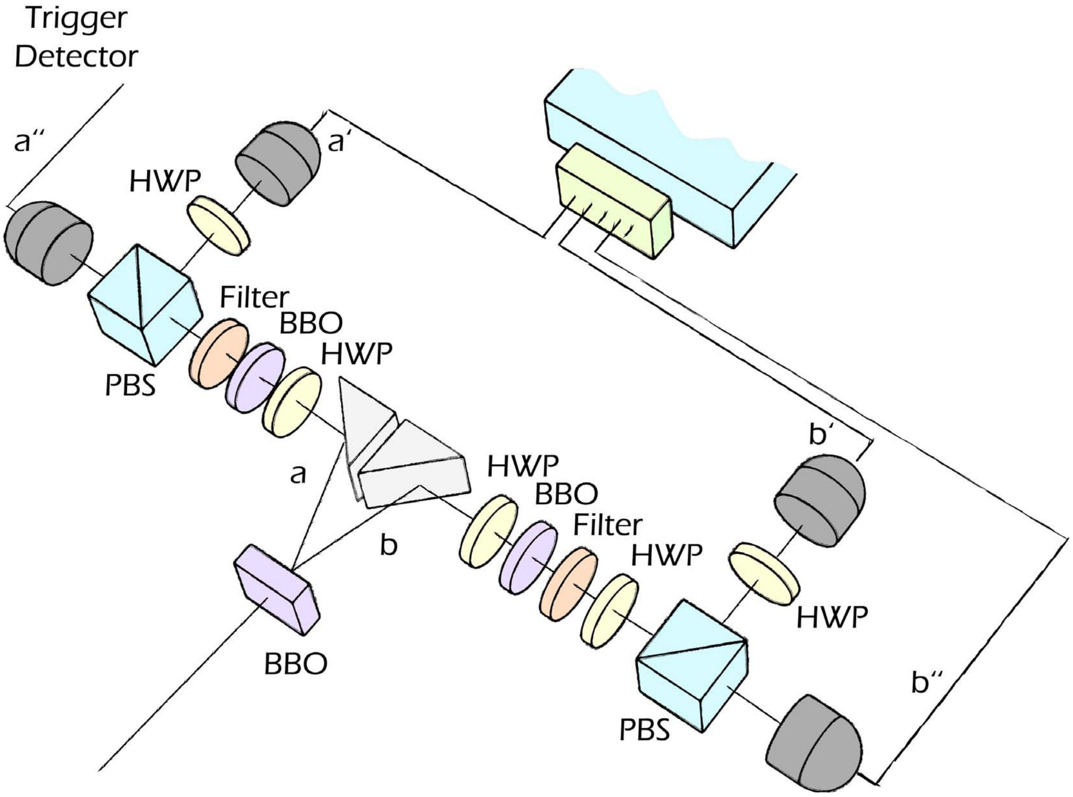

FIGURE 3.12: **State Generation.**The generated state is coupled into the spatial modes a and b which are split by a polarizing beam splitter (PBS). Half wave plates (HWP) in the reflected output ports of the PBS cubes ensure that all photons exhibit the same polarization when they are coupled into the modes a'', a', b', and b''. This setup allows to herald three indistinguishable photons in the modes a', b', and b'' with a successful trigger event in mode a''.

To make sure that only the desired input state is measured, post-selection on a trigger event is necessary. A detection of a photon in the trigger detector a'' represents either the state $|HH\rangle_{b''}$ or $|V\rangle_{a'}|V\rangle_{b'}|H\rangle_{b''}$. Only the latter case guarantees that three modes a', b', and b'' are occupied with one single photon.The first case represents mode b'' occupied with two photons and mode b' occupied with vacuum. Post-selection on a four-fold coincidence between the modes a'', a', b', and b'' means taking only the events into account, where only one photons enters each input mode.

3.2.8 Making measurements

The down-conversion source is pumped with a power of 700 mW to generate two photon pairs, which are then split into four spatial couplers. Three of these modes, are directly coupled to the waveguide chip. The fourth mode is connected to a trigger detector. The aim is to measure six different points on a three-dimensional coincidence landscape.

	$\Delta\tau_1$	$\Delta\tau_2$
P1	0 fs	0 fs
P2	0 fs	-1000 fs
P3	-300 fs	-300 fs
P4	-1000 fs	-1000 fs
P5	-1000 fs	0 fs
P6	-1000 fs	1000 fs

The procedure is the same for all six points. The relative temporal delay has to be set before the measurement starts. Our FPGA logic is programmed in a manner that it measures coincidences at three of the five output ports and a trigger event, see figure 3.13. There exist 10 different ways to inject three photons into a five-moded network. This implies that these three photons can exit the interferometer in 10 different ways. All together there are 100 combinations of input and output ports which specify in each case a 3×3 sub-matrix R. In the experiment we fixed the input state to the input ports 1,2 and 4. Like this we obtained 10 coincidence landscapes as shown in figure 3.1.

At first we collected data for every single point individually but our setup was not very stable, namely we could measure a noticeable drift. This drift showed a constant decrease of coincidences over the measurement time. The reason for this is that the setup becomes misaligned. In our case this happened because the temperature in the lab was fluctuating drastically. This means the coincidence counts for the first measured point were much better than the one for the last measured point. The results were therefore not comparable. The solution for

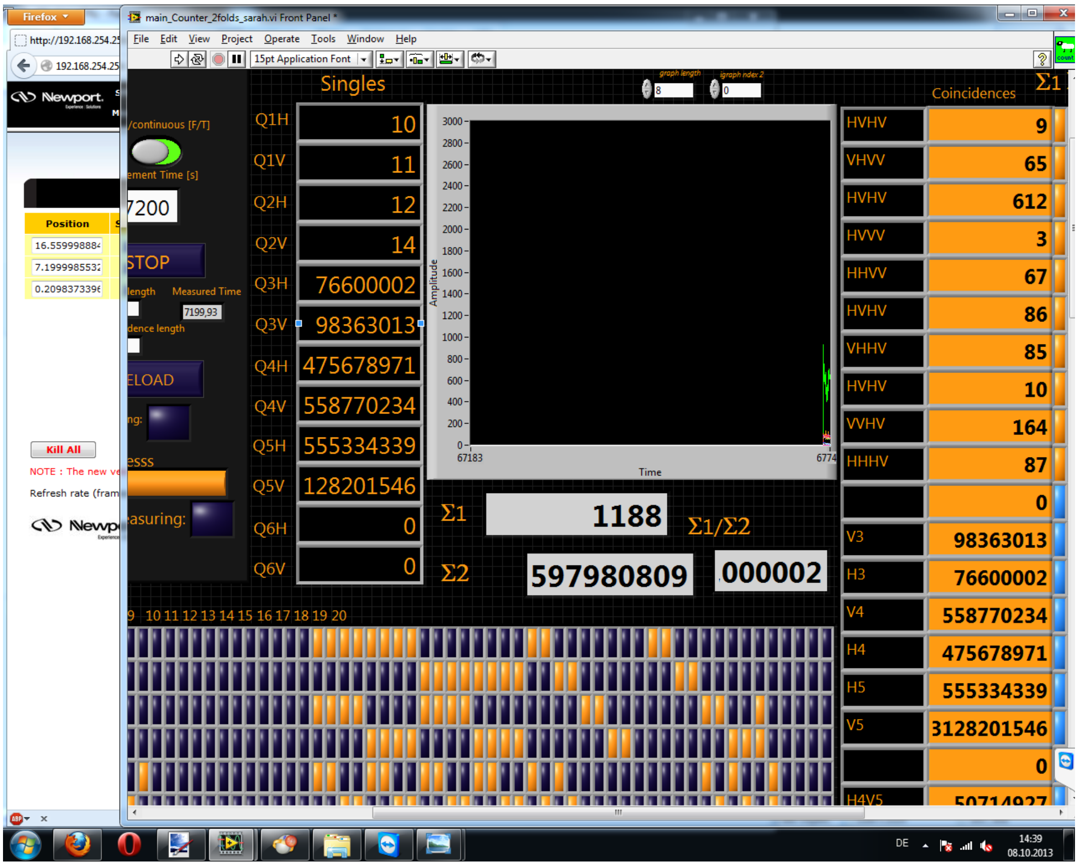
Firefox
main_Counter_2folds_sarah.vi Front Panel *
File Edit View Project Operate Tools Window Help
15pt Application Font
Newport.
Kill All
STOP
ELOAD
Singles
Coincidences
Amplitude
Time
graph length
graph nder 2
9 10 11 12 13 14 15 16 17 18 19 20

Position
16.55999888
7.1999985532
0.2098373396

Measurement Time [s]: 7200
Measured Time: 7199,93

Singles
Q1H 10
Q1V 11
Q2H 12
Q2V 14
Q3H 76600002
Q3V 98363013
Q4H 475678971
Q4V 558770234
Q5H 555334339
Q5V 128201546
Q6H 0
Q6V 0

Σ1 1188
Σ2 597980809
Σ1/Σ2 000002

Coincidences Σ1
HVHV 9
VHVV 65
HVHV 612
HVVV 3
HHVV 67
HVHV 86
VHHV 85
HVHV 10
VVHV 164
HHHV 87
0
V3 98363013
H3 76600002
V4 558770234
H4 475678971
H5 555334339
V5 3128201546
0

FIGURE 3.13: **Screen shot of the measurement program.** On the left side the 10 output combinations are recorded as coincidences, where the forth "V" stands for a count at the trigger detector. Beneath, the single counts for all five outputs (V3, H3, V4, H4, H5) and the trigger detector (V5) are measured. $\sum 1$ shows the sum of the coincidences and $\sum 2$ the sum of all single counts. On the right side, in a different window, the position of the delays can be set. This can all be done via remote control.

this problem was to measure all points consecutively to each other in one run. Such a measurement run is defined by recording P1 to P6 consecutively for 2 hours each. With this measurement method we could again see a drift over the 12 hours run, so we reversed the order every second time (P6 to P1) to compensate this drift. After every run the setup was realigned to optimize the maximal count rate. All in one we repeated the measurement 19 times to achieve reasonable statistics. This result in a total measurement time of 228 hours. The experimental data can be found in the appendix.

3.3 Results

3.3.1 Characterization of the Network

In order to compare the experimentally obtained data to our theoretical model one must first reconstruct the 5×5 unitary transition matrix, which describes the optical network. Although we have a theoretical description of the interferometer, it is important to extract the actual unitary transformation experimentally, because even advanced writing precision can introduce small deviations from the initially targeted values of individual elements. In case of our 10 cm long chip this writing precision is limited to around 50 nm over the whole length. Because our network is a Mach-Zehnder decomposition small deviations of individual elements may add up to a noticeable deviation in the overall transformation. The splitting ratio of individual directional couplers is set by their mode separation and coupling length. These two variables are unaffected because they are three orders of magnitude bigger than the position precision. A problem appears when it comes to length fluctuations due to the positioning precision. This causes unintended phase shifts, which can lead to a phase shifter that stretches over the whole length of the waveguide. All these influences need to be considered, so it is crucial to evaluate the actually implemented unitary.

We use a chi-square test, which is a goodness of fit protocol, as a quality indicator for our network characterization. It provides information about how well the observation fits with the model. In other words, it is a measure of the discrepancy between observed values and the values predicted by the model. The χ^2 is defined as,

$$\chi^2 = \sum \frac{(E - T)^2}{\sigma^2}, \tag{3.12}$$

where E is the experimental data, T is the theoretical prediction and σ^2 is the variance of the measured data. In our experiment we use the reduced chi squared method [41] as it enables data sets of different lengths and models with different numbers of variables to be compared with one another fairly. The reduced chi-squared is defined as the chi-squared divided by the number of the degrees of freedom,

$$\chi^2_{red} = \frac{1}{\nu} \sum \frac{(E-T)^2}{\sigma^2}. \tag{3.13}$$

Here, $\nu = N - n - 1$ is the number of degrees of freedom, where N is the number of data sets and n the number of fitted parameters. We interpret the results of equation (3.13) in the following way,

- $\chi^2_{red} = 1$ states a good result and the model describes the data, or rather the match between estimates and observations is in accordance with the error variance.
- $\chi^2_{red} > 1$ means that the fit does not fully cover the model, which can be caused by underestimating the error variance.
- $\chi^2_{red} < 1$ indicates that either the error variance has been overestimated or the influence of noise is to high, which is therefore fitted by the model.

For the characterization method in this experiment we used two-photon states, emitted from a SPDC source and injected into different input modes of the optical network. This procedure builds on the one which is used in [25, 42].

In the following is described what we need for the reconstruction, how we build the reconstruction and how good the quality of the reconstructed unitary is [35].

We already defined our optical interferometric network as a 5×5 unitary matrix. The transformation of this matrix can be reconstructed via visibilities of two-photon HOM-dips. This is done by injecting two photons into the waveguide chip, namely in any combination of two of its five possible input modes. An indicator for the quality of a HOM-dip is its the resulting visibility. The general formula for calculating a visibility is

$$V = \frac{I_{max} - I_{min}}{I_{max} + I_{min}}, \tag{3.14}$$

where I is the intensity and in our case equatable with coincidences. I_{max} is therefore the coincidence rate when the photons are distinguishable and I_{min} when they are indistinguishable.

For a five moded interferometer there exist ten possible combinations for two photons to be injected on the input and also 10 possible combinations how they exit the network on the output. This results in a sum of 100 visibilities to calculate. As shown in figure 3.8, the input 5 of our waveguide never couples to the output $1'$. This leads to a visibility of zero for the input combinations $15, 25, 35, 45$ and the output combinations $1'5', 2'5', 3'5', 4'5'$. So the unitary transformation is reconstructed from $100 - 16 = 84$ non-zero visibilities of 2×2 submatrices. For recording a HOM-dip it is essential that the two indistinguishable photons enter the integrated network at the same time. Since the delay lines in our experiment can be varied in their length, the position where the photons become indistinguishable in their temporal delay is identified as follows. One input mode is kept fixed and the other one translated until a dip can be recorded by our measurement program. When a dip was localized we defined a start point, where the two photons are still indistinguishable and an end point where they become indistinguishable again. The recorded HOM-dip in between these two positions is split into 30 measurement points with a step width of 66 fs. Each point was recorded for 800 seconds and the coincidences are read out by our FPGA-logic. For all input combinations we recorded 10 dips simultaneously. As an example for one measurement run, the recorded 10 dips for the input combination 34 is shown in figure 3.14.

Figure 3.14 shows just the raw data. This has to be modeled for proper analysis.

At first it is necessary to take the spectral shape of the photons into account. We measure that with a single-photon spectrometer (Ocean Optics QE6500) and find that it is a good approximation of a Gaussian shape. In an experiment the involved photons never have the exact spectral function, so the resulting mismatch has to be considered. The photons used for the characterization measurement exhibit a central wavelength and spectral bandwidth of $\lambda_1 = 789.05\,\text{nm}$,

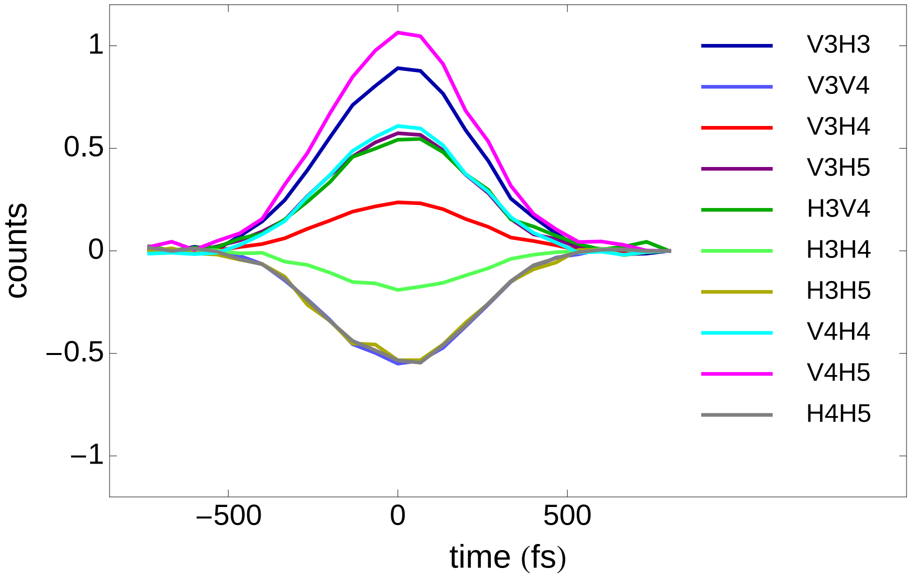

FIGURE 3.14: **Example for a set of HOM dips.**Two photons are injected into the input ports 3 and 4 of the integrated network. At the output the 10 possible output combinations for two photons are recorded. The figure shows the coincidence rates for the 10 combinations along a certain time delay.

$\Delta\lambda_1 = 2.9\,\text{nm}$, and $\lambda_2 = 788.60\,\text{nm}$, $\Delta\lambda_2 = 2.9\,\text{nm}$ respectively.

Another important thing which can be harmful for the analysis is the contribution of higher-order emission and noise. In case of a four-fold emission this can happen if two photons in one input mode leave the network in two separate output modes, while the two photons in the other input mode are lost. To rate the contribution of such noise we blocked both inputs respectively and recorded the two-photon coincidences on the output. These signals are labeled HO_1 and HO_2 and have to be subtracted from the data. Noise arising from background light and electrical noise is combined in the background coincidence rate d. The corrected coincidence count rate N_c can be written as inverted Gaussian,

$$\begin{aligned} N_c(t) =& (1 + T * t)(Y_0 + A\frac{2\sigma_1\sigma_2}{\sigma_1^2+\sigma_2^2}\exp\left(-\frac{(\Omega_1-\Omega_2)^2 + 4\sigma_1^2\sigma_2^2(t-t_c)^2}{2(\sigma_1^2+\sigma_2^2)}\right) \\ & - (HO_1 + HO_2 - d))\ , \end{aligned} \tag{3.15}$$

with Y_0 as linear offset, A as the amplitude, t_c as the central time and T as drift parameter. These are the best fit parameters to the experimental data and important for the final formula for the visibility:

$$V = 1 - \frac{Y_0 + A}{Y_0} \; . \tag{3.16}$$

With this method 84 out of 100 non-zero visibilities V and their standard deviation σ are extracted. The overlap between experimental data and theoretical model results in an $\chi^2_{\text{red}} = 1.74$.

For the reconstruction of the unitary transformation of our optical network we used not just the two-photon interference visibilities [42] but also single-photon transmission probabilities. The real entries of the matrix are estimated from the single-photon data while the imaginary entries are reconstructed from the two-photon visibilities [35]. The parameters of the interferometric network should give an optimal fit to the measured visibilities. This can be achieved by using a least square optimization weighted with the standard errors of the experimental data. All in one the 19 parameters consist of eleven phase shifters $\phi_1, \phi_2, \ldots \phi_{11}$ and eight beam splitters $\beta_1, \beta_2, \ldots \beta_8$. For finding the best fit set of parameters, a Matlab program is used to minimize the equation

$$V_{\text{opt}} = \sum_{i=1}^{84} \frac{\left(V_i^{(\text{exp})} - V_i^{(\text{th})}\right)^2}{\sigma_i^2 \Gamma} \; , \tag{3.17}$$

where $V_i^{(\text{th})}$ is the theoretical value of the visibility calculated from the unitary model of the interferometer and Γ is a constant value equal to (number of data sets in visibilities - number of parameters - 1)=2314.

Equation (3.17) looks similar to a reduced χ^2 but needs to be interpreted in a different way. We want to achieve a value close to 0. That indicates good agreement between the experimentally extracted visibilities and the theoretically predicted visibilities. In this case the result is $V_{\text{opt}} = 0.351$. The 5×5

reconstructed matrix U_5 we get by using the procedure explained above is

$$U_5 = \begin{pmatrix} 0.032-0.337i & 0.072+0.820i & -0.278-0.106i & 0.123-0.322i & 0 \\ 0.011+0.275i & -0.386+0.186i & -0.135+0.207i & -0.784-0.150i & 0.012-0.204i \\ -0.776-0.233i & -0.294+0.002i & -0.268-0.016i & 0.027+0.352i & -0.248-0.015i \\ 0.144-0.261i & -0.152-0.084i & -0.139+0.084i & -0.133-0.009i & 0.020+0.845i \\ 0.223+0.123i & 0.072-0.129i & -0.793-0.027i & 0.087+0.307i & 0.412-0.112i \end{pmatrix}. \tag{3.18}$$

This matrix can now be used to predict an output probability $P_{11}^{(}theory)$ for any two-photon input combination. The coincidence count rate N_c can then be rewritten as

$$N_c^{(\text{theory})}(t) = N_0(1+T)P_{11}^{(\text{theory})}(t-t_c), \tag{3.19}$$

where N_0 can be interpreted as background and t_c and T are again parameters for the central time and the drift. These parameters are used to find the best fit to the experimental data. The χ^2_{red} is expressed and calculated by

$$\chi^2_{\text{red}} = \sum_{i=1}^{m} \frac{\left(N_{c,i}^{(\text{experiment})} - N_{c,i}^{(\text{theory})}\right)^2}{\nu\epsilon_i^2}, \tag{3.20}$$

where $m = 3030$, $\nu = 2909$ and ϵ_i is the error for the corresponding data point. The experimental data, which is already corrected for higher order emission, is expressed by $N_{c,i}^{(\text{experiment})}$. The resulting χ^2_{red} between the data and the predicted coincidence counts using U_5 is $\chi^2_{\text{red}} = 2.086$.

3.3.2 Coincidence landscapes

We use the transition matrix obtained in equation (3.18) to construct coincidence landscapes for one input and the corresponding 10 output combinations. Figure 3.15 shows these landscapes. The troughs or ridges outside the central region are characterized by pairwise temporal indistinguishability ($\Delta\tau_1 = \Delta\tau_2$,

$\Delta\tau_1 = 0$, and $\Delta\tau_2 = 0$). These result from non-classical interference between two of the three photons. The weightings of the permanent, determinant and immanants in the output probability is dependent of the temporal overlap of these photons. All the remaining areas form a plateau, which we refer to as "background". There all photons exhibit complete temporal distinguishability, and subsequently classical behavior. The different regions of the coincidence landscape can be connected mathematically using equation (2.26). In the center all photons are indistinguishable and should actually cause destructive interference of 54 of the 60 terms. This would lead to a contribution of just the permanent in the output distribution.

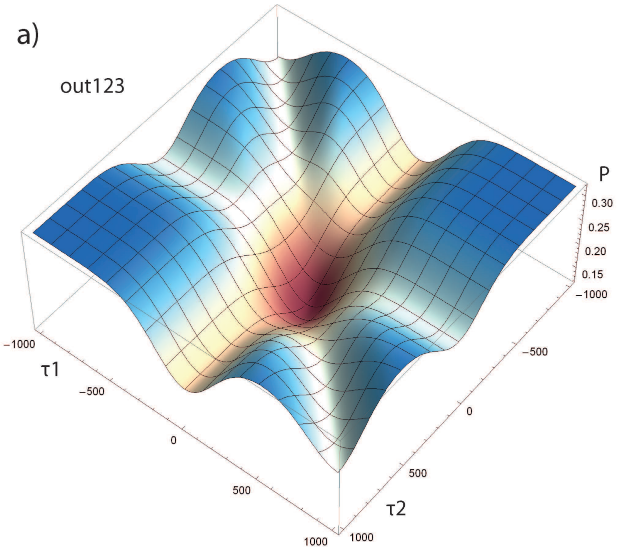

FIGURE 3.15: **Coincidence landscape.** This figure shows the illustration of the first of the 10 resulting coincidence landscapes. In the following all of the other landscapes are shown as well. One can see immediately that the different output combinations show distinct shapes.

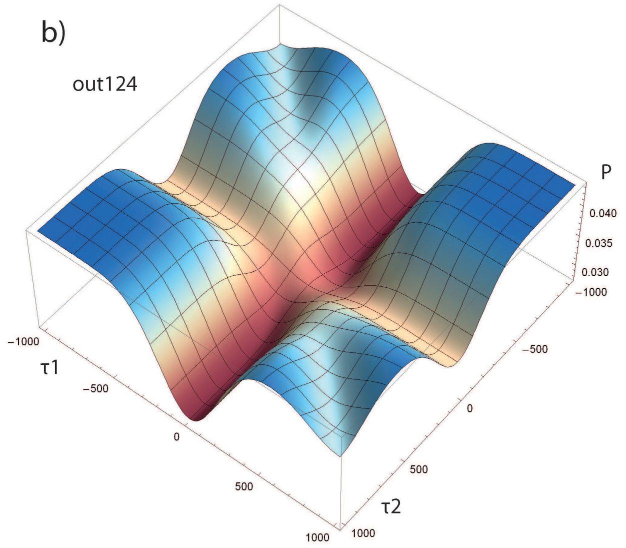
b)
out124
P
0.040
0.035
0.030
−1000
τ1
−500
0
500
1000
−1000
−500
0
500
τ2
1000

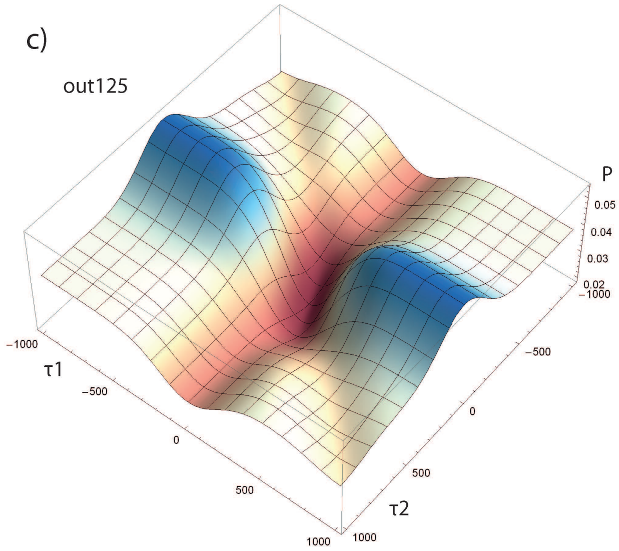
c)
out125
P
0.05
0.04
0.03
0.02
−1000
τ1
−500
0
500
1000
−1000
−500
0
500
τ2
1000

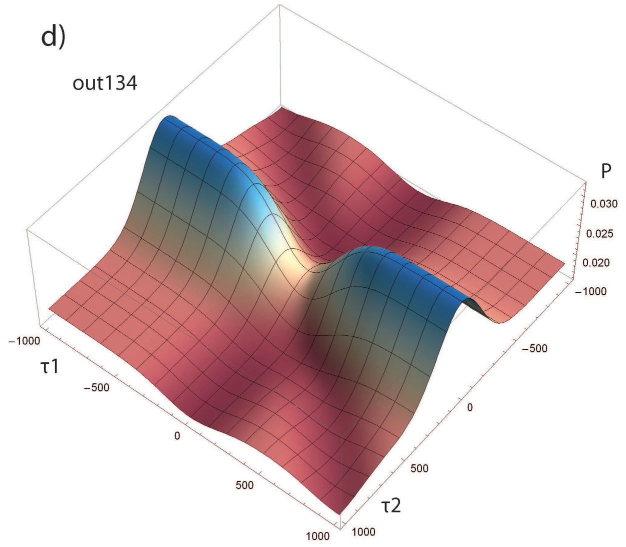
d)
out134
P
0.030
0.025
0.020
−1000
τ1
−500
0
500
1000
−1000
−500
0
500
τ2
1000

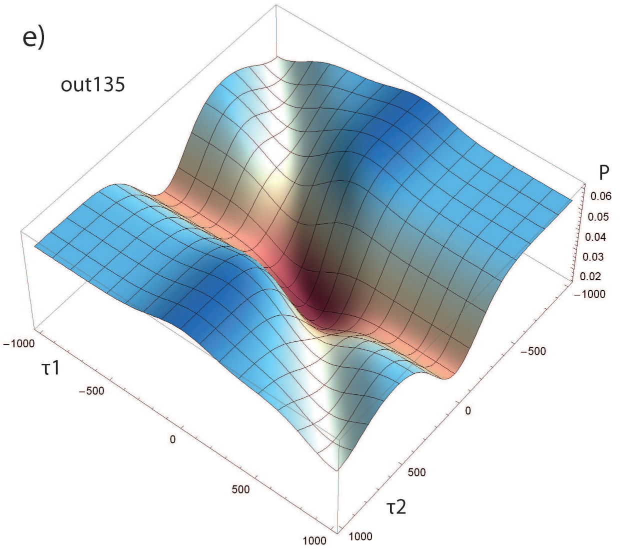
e)
out135
P
0.06
0.05
0.04
0.03
0.02
−1000
−500
0
500
1000
τ2
−1000
τ1
−500
0
500
1000

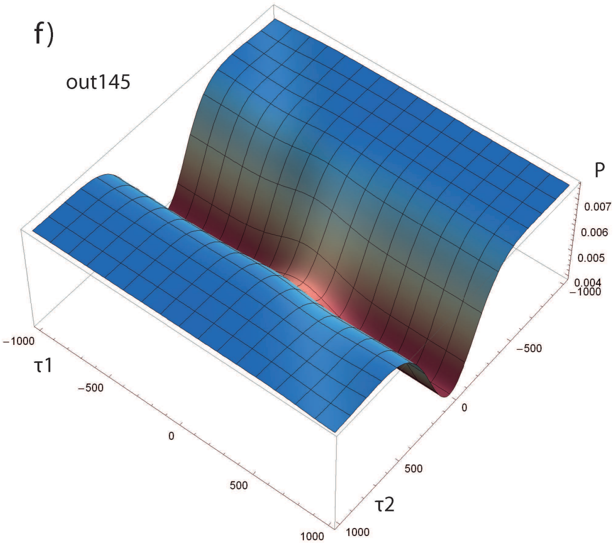
f)
out145
P
0.007
0.006
0.005
0.004
−1000
−500
0
500
1000
τ2
−1000
τ1
−500
0
500
1000

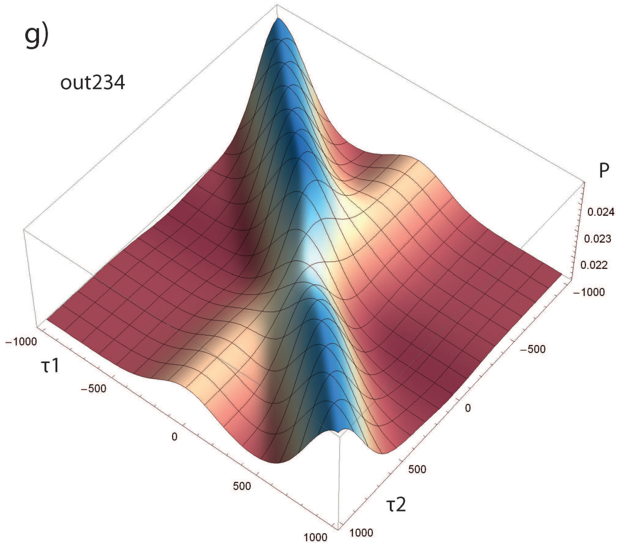
g)
out234
P
0.024
0.023
0.022
−1000
−500
0
500
1000
τ2
−1000
τ1
−500
0
500
1000

h)

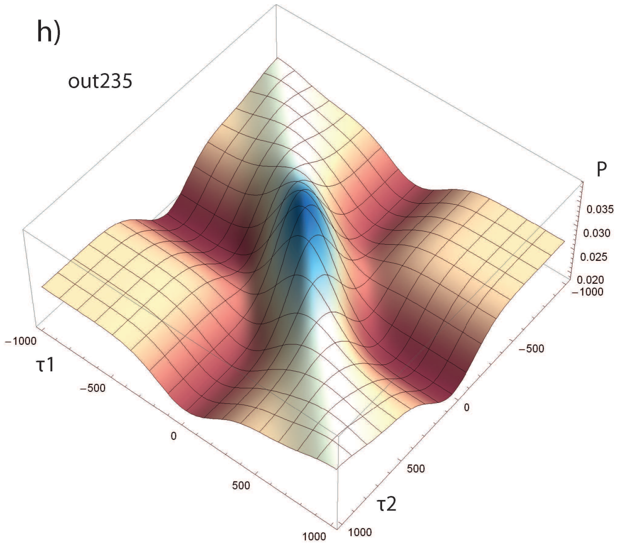
out235
P
0.035
0.030
0.025
0.020
−1000
−500
0
500
1000
τ2
−1000
τ1
−500
0
500
1000

i)

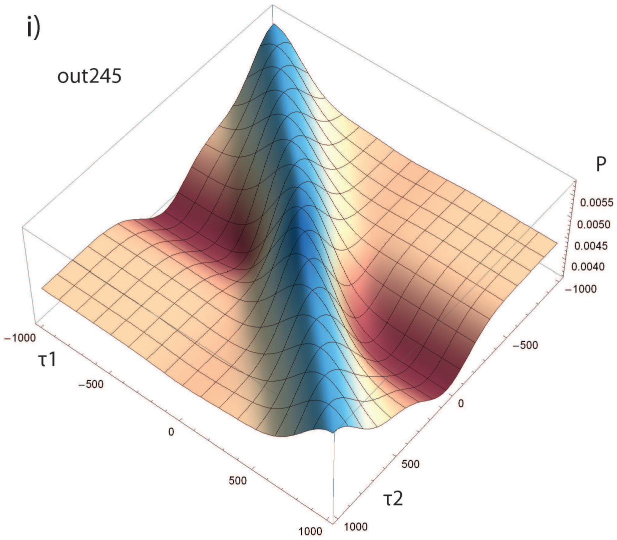
out245
P
0.0055
0.0050
0.0045
0.0040
−1000
−500
0
500
1000
τ2
−1000
τ1
−500
0
500
1000

j)

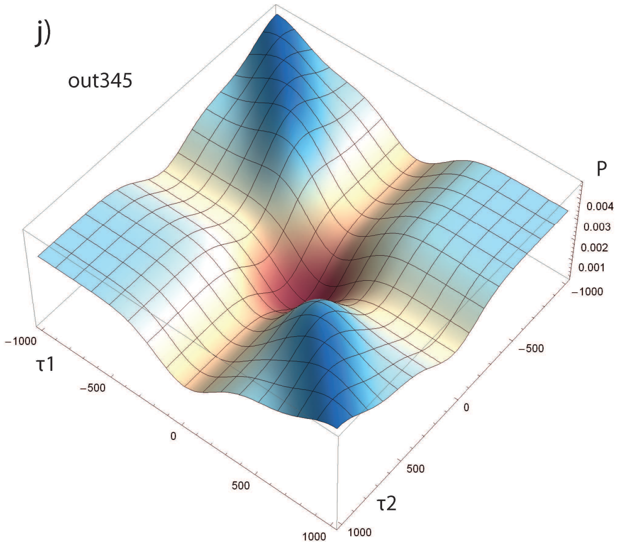
out345
P
0.004
0.003
0.002
0.001
−1000
−500
0
500
1000
τ2
−1000
τ1
−500
0
500
1000

3.3.3 Comparing data with our theoretical model

Here we compare the theoretical predictions from equation (2.26), as plotted in figures 3.15, a) - j), with our experimental data for the 10 different output probabilities using all six measurement points.

The experimental coincidences at each point are normalized such that their sum is equal to one. Data points represent the mean of 19 measurements with error bars corresponding to the standard error of each measurement. The theoretical values are also normalized so that their sum at each point is equal to one. This enables us to compare them with the experimental results independently of the total number of counts expected. Figure 3.16 shows a comparison of the experimental findings to the theoretical model. The complete data can be found in the appendix.

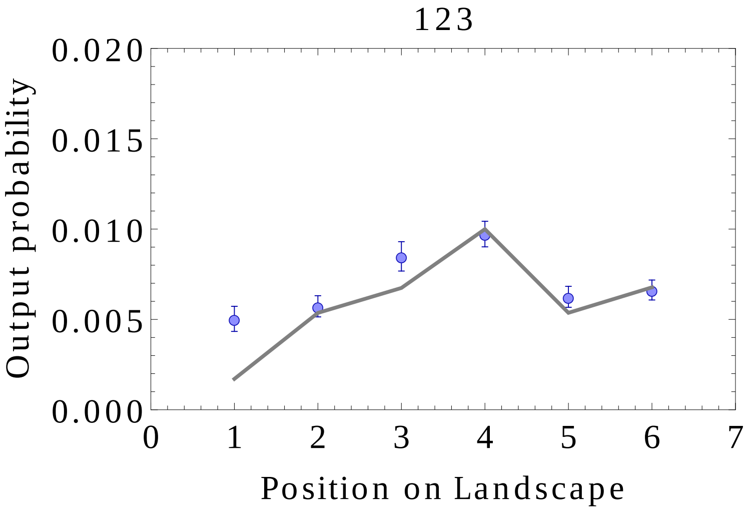

FIGURE 3.16: **Results.** These Plots show the overlap between the theoretical model and the experimentally obtained data. The blue dots represent the mean value of the 19measurement runs for the six points on a coincidence landscape. The gray line shows the theoretically predicted values. Every plot corresponds to one of the 10 coincidence landscapes respectively.

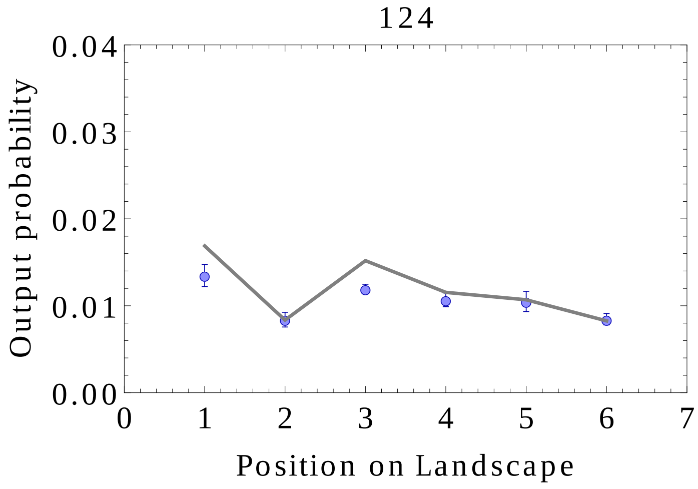
124

Output probability
0.00
0.01
0.02
0.03
0.04
0
1
2
3
4
5
6
7
Position on Landscape

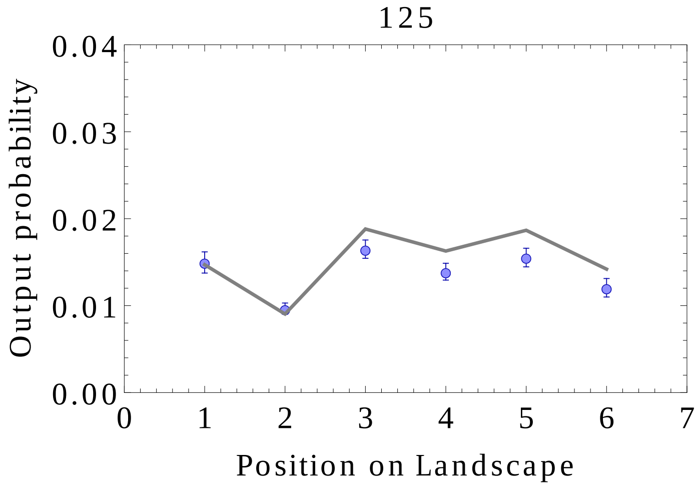
125

Output probability
0.00
0.01
0.02
0.03
0.04
0
1
2
3
4
5
6
7
Position on Landscape

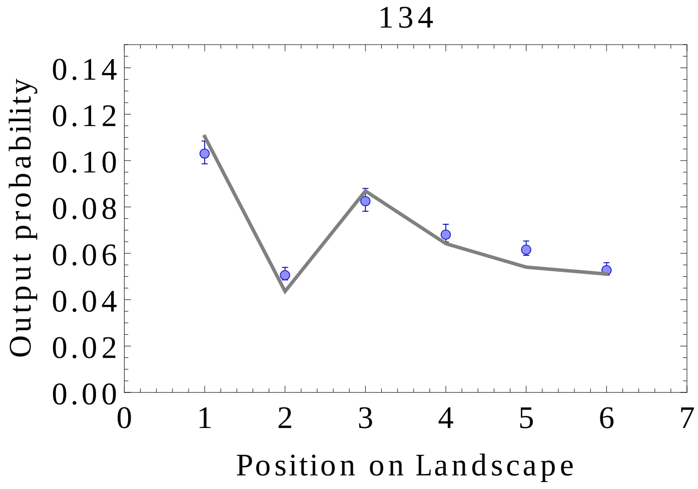
134

Output probability
0.00
0.02
0.04
0.06
0.08
0.10
0.12
0.14
0
1
2
3
4
5
6
7
Position on Landscape

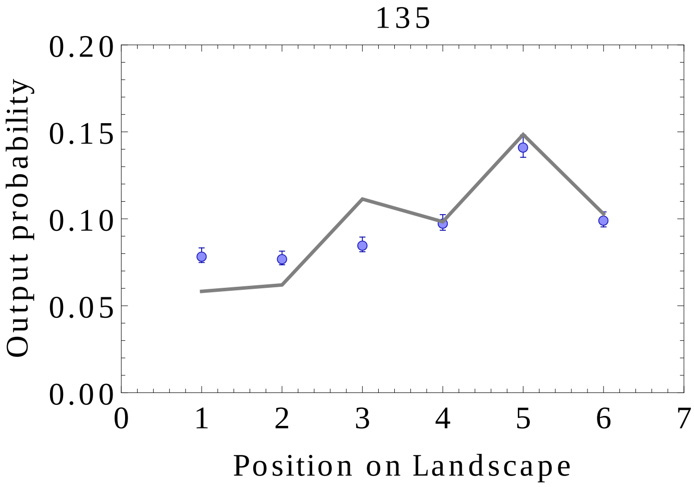
135
Output probability
0.20
0.15
0.10
0.05
0.00
0
1
2
3
4
5
6
7
Position on Landscape

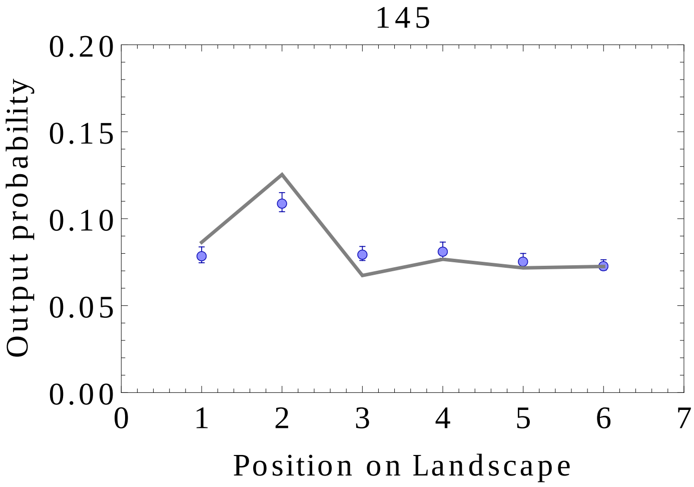
145
Output probability
0.20
0.15
0.10
0.05
0.00
0
1
2
3
4
5
6
7
Position on Landscape

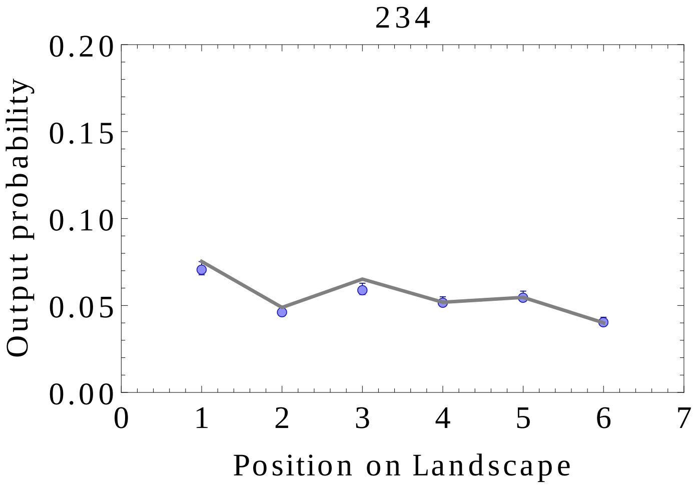
234
Output probability
0.20
0.15
0.10
0.05
0.00
0
1
2
3
4
5
6
7
Position on Landscape

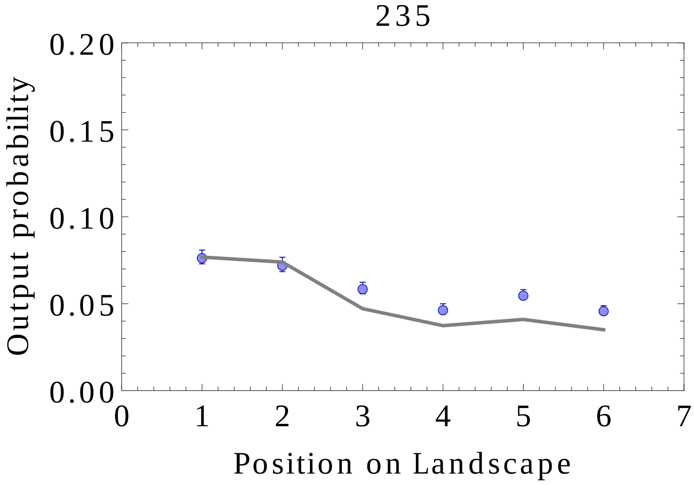
235
Output probability
0.20
0.15
0.10
0.05
0.00
0
1
2
3
4
5
6
7
Position on Landscape

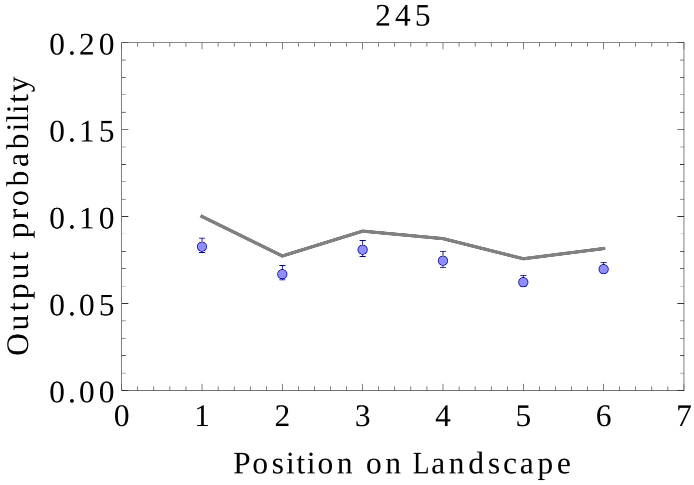
245
Output probability
0.20
0.15
0.10
0.05
0.00
0
1
2
3
4
5
6
7
Position on Landscape

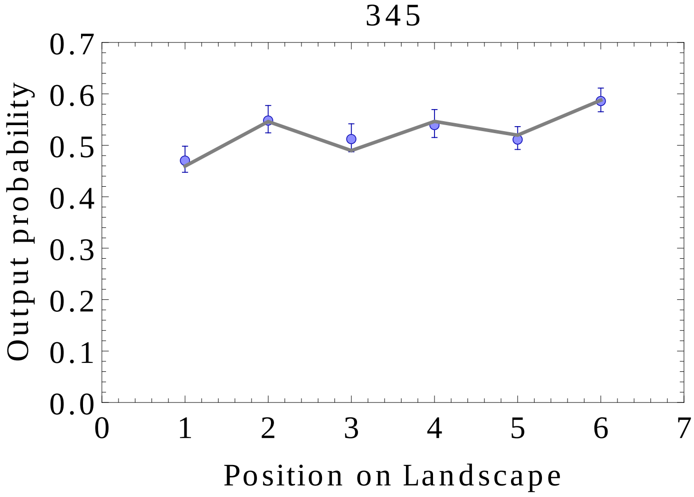
345
Output probability
0.7
0.6
0.5
0.4
0.3
0.2
0.1
0.0
0
1
2
3
4
5
6
7
Position on Landscape

Our results presented in figure 3.16 shows good, qualitative agreement between theory and experiment. Slight deviations occur due to the uncertainty in the reconstruction of the unitary. We find that the output probability is proportional to the permanent of the transition matrix, as in earlier boson sampling experiments [23–26]. We also find that the introduction of additional terms proportional to the immanants of the transition matrix provide an improved description of the output distributions.

Conclusion

Boson sampling is a passive optical scheme which lacks the possibility for error correction. Its success therefore relies on the quality of the measurements which can be performed. In this thesis I have experimentally investigated the influence of the two main sources of error in a boson sampling experiment, namely the incorrect characterization of the interferometer and the inadequate preparation of the input state. Concerning the characterization of the interferometric network, an improved method of transition matrix reconstruction is presented resulting in a better description of the experimental results of boson sampling. Furthermore a detailed description of the input photon distinguishability is investigated. In early boson sampling experiments only the permanent of the transition matrix was used to describe the output probability, assuming only completely indistinguishable photons were used. Under realistic experimental conditions this is a significant simplification and in order to account for the finite distinguishability of the photons the immanants and the determinant of the transition matrix are required, not simply the permanent.

This method leads to a much better understanding of the output probability distribution of the interferometric network and has important implications for all multi-photon experiments which rely on non-classical interference of photons in linear optical networks.

Appendix A

Mathmatical Background

A.1 Derivation of the two-photon overlap integral

In section 2.2.2 we introduced the spectral overlap integral for two photons injected into a network. For the experiment presented in this thesis it is necessary to express this overlap integral in terms of permanents and determinants. This will be shown step by step in this section.

The spectral overlap integral for two photons can be written as

$$\begin{aligned} P_{11}(\Delta\tau) &= \int d\omega \int d\omega' \left| \langle 11| U^\dagger a_1^\dagger(\omega) a_2^\dagger(\omega') |0\rangle \right|^2 \\ &= \int d\omega \int d\omega' \left| \langle 0| a_1(\omega) a_2(\omega') U |11\rangle \right|^2 \end{aligned} \tag{A.1}$$

where $a_1^\dagger(\omega)$ and $a_2^\dagger(\omega')$ are creation operators in two spatial modes of a network which is defined by the 2×2 matrix

$$U = \begin{pmatrix} U_{11} & U_{12} \\ U_{21} & U_{22} \end{pmatrix}. \tag{A.2}$$

Furthermore we need the definition for the two-photon input state

$$|11\rangle = (\hat{A}_1^\dagger(\alpha_1)e^{i\omega_1\tau_1})(\hat{A}_2^\dagger(\alpha_2)e^{i\omega_2\tau_2})|0\rangle, \tag{A.3}$$

where

$$\hat{A}^\dagger(\alpha) = \int\limits_0^\infty d\omega\alpha(\omega)\hat{a}^\dagger(\omega) \tag{A.4}$$

and the photons spectral function

$$|\alpha(\omega_i)|^2 = \frac{1}{\sqrt{2\pi}\sigma_i}\exp\left(-\frac{(\omega_i - \Omega_i)^2}{2\sigma_i^2}\right), \tag{A.5}$$

where ω_i is the angular frequency of the i^{th} photon and Ω_i and σ_i are the mean frequency and standard deviation of the i^{th} photon distribution respectively. Now the generalized two-photon input state can be written as

$$|11\rangle = \int\limits_0^\infty\int\limits_0^\infty d\omega_1 d\omega_2 \alpha_1(\omega_1)\alpha_2(\omega_2)a_1^\dagger(\omega_1)a_2^\dagger(\omega_2)e^{i\omega_1\tau_1 + i\omega_2\tau_2}|0\rangle. \tag{A.6}$$

This expression can now be used to calculate the amplitude from equation (A.2).

$$
\begin{aligned}
&\langle 0|a_1(\omega)a_2(\omega')U|11\rangle = \qquad\qquad\qquad\qquad\qquad\qquad \text{(A.7)}\\
&= \langle 0|a_1(\omega)a_2(\omega')U \int_0^\infty\int_0^\infty d\omega_1 d\omega_2 \alpha_1(\omega_1)\alpha_2(\omega_2)a_1^\dagger(\omega_1)a_2^\dagger(\omega_2)e^{i\omega_1\tau_1+i\omega_2\tau_2}|0\rangle\\
&= \int_0^\infty\int_0^\infty d\omega_1 d\omega_2 \alpha_1(\omega_1)\alpha_2(\omega_2)e^{i\omega_1\tau_1+i\omega_2\tau_2}\langle 0|a_1(\omega)a_2(\omega')Ua_1^\dagger(\omega_1)a_2^\dagger(\omega_2)|0\rangle\\
&= \int_0^\infty\int_0^\infty d\omega_1 d\omega_2 \alpha_1(\omega_1)\alpha_2(\omega_2)e^{i\omega_1\tau_1+i\omega_2\tau_2}\langle 0|a_1(\omega)a_2(\omega')\\
&\qquad\qquad \times \left[U_{11}a_1^\dagger(\omega_1)+U_{21}a_2^\dagger(\omega_1)\right]\left[U_{12}a_1^\dagger(\omega_2)+U_{22}a_2^\dagger(\omega_2)\right]|0\rangle\\
&= \int_0^\infty\int_0^\infty d\omega_1 d\omega_2 \alpha_1(\omega_1)\alpha_2(\omega_2)e^{i\omega_1\tau_1+i\omega_2\tau_2}\langle 0|a_1(\omega)a_2(\omega')\\
&\qquad\qquad \times \left[U_{11}U_{22}a_1^\dagger(\omega_1)a_2^\dagger(\omega_2)+U_{21}U_{12}a_2^\dagger(\omega_1)a_1^\dagger(\omega_2)\right]|0\rangle\\
&= \int_0^\infty\int_0^\infty d\omega_1 d\omega_2 \alpha_1(\omega_1)\alpha_2(\omega_2)e^{i\omega_1\tau_1+i\omega_2\tau_2}\langle 0|a_1(\omega_1)a_2(\omega_2)\\
&\qquad \times \left[U_{11}U_{22}\delta(\omega-\omega_1)\delta(\omega'-\omega_2)+U_{21}U_{12}\delta(\omega'-\omega_1)\delta(\omega-\omega_2)\right]|0\rangle\\
&= U_{11}U_{22}\alpha_1(\omega)\alpha_2(\omega')e^{i\omega\tau_1+i\omega'\tau_2}+U_{21}U_{12}\alpha_1(\omega')\alpha_2(\omega)e^{i\omega'\tau_1+i\omega\tau_2}
\end{aligned}
$$

This last term is then inserted into equation (A.2), to continue the calculation.

$$
\begin{aligned}
P_{11}(\Delta\tau) =& \int d\omega \int d\omega' \Big|\langle 0|a_1(\omega)a_2(\omega')U|11\rangle\Big|^2 \qquad (A.8)\\
=& \int d\omega \int d\omega' \Big|U_{11}U_{22}\alpha_1(\omega)\alpha_2(\omega')e^{i\omega\tau_1+i\omega'\tau_2} + U_{21}U_{12}\alpha_1(\omega')\alpha_2(\omega)e^{i\omega'\tau_1+i\omega\tau_2}\Big|^2\\
=& |U_{11}|^2|U_{22}|^2 + |U_{21}|^2|U_{12}|^2\\
+& \int d\omega \int d\omega' \alpha_1(\omega)\alpha_2(\omega')e^{i\omega\tau_1+i\omega'\tau_2}\, U_{11}U_{22}U_{21}^*U_{12}^*\alpha_1(\omega')\alpha_2(\omega)e^{-i\omega'\tau_1-i\omega\tau_2}\\
+& \int d\omega \int d\omega' \alpha_1(\omega')\alpha_2(\omega)e^{i\omega'\tau_1+i\omega\tau_2}\, U_{21}U_{12}U_{11}^*U_{22}^*\alpha_1(\omega)\alpha_2(\omega')e^{-i\omega\tau_1-i\omega'\tau_2}\\
=& |U_{11}|^2|U_{22}|^2 + |U_{21}|^2|U_{12}|^2\\
+& \Big[\int d\omega\alpha_1(\omega)\alpha_2(\omega)e^{i\omega\tau_1-i\omega\tau_2} \int d\omega'\alpha_2(\omega')\alpha_1(\omega)e^{i\omega'\tau_2-i\omega'\tau_1}\Big]\, U_{11}U_{22}U_{21}^*U_{12}^*\\
+& \Big[\int d\omega\alpha_2(\omega)\alpha_1(\omega)e^{i\omega\tau_2-i\omega\tau_1} \int d\omega'\alpha_1(\omega')\alpha_2(\omega)e^{i\omega'\tau_1-i\omega'\tau_2}\Big]\, U_{21}U_{12}U_{11}^*U_{22}^*
\end{aligned}
$$

By using the definition for the spectral function for a photon from (A.5) we can write equation (A.8) as

$$
\begin{aligned}
P_{11}(\Delta\tau) =& \Big[|U_{11}|^2|U_{22}|^2 + |U_{21}|^2|U_{12}|^2\Big] + \Big[U_{11}U_{22}U_{21}^*U_{12}^* + U_{21}U_{12}U_{11}^*U_{22}^*\Big] \qquad (A.9)\\
&\times \frac{\sigma_1\sigma_2}{\sigma_1^2+\sigma_2^2}\exp\left(-\frac{(\Omega_1-\Omega_2)^2}{2(\sigma_1^2+\sigma_2^2)} - 2(\tau_1-\tau_2)^2\frac{\sigma_1^2\sigma_2^2}{\sigma_1^2+\sigma_2^2}\right)
\end{aligned}
$$

Now we want to write equation (A.9) in terms of permanents and determinants. This can be done by using

$$
\begin{aligned}
\mathrm{per}(U) &= U_{11}U_{22} + U_{21}U_{12} \qquad & \mathrm{per}(U) + \det(U) &= 2U_{11}U_{22} \qquad (A.10)\\
\det(U) &= U_{11}U_{22} - U_{21}U_{12} \qquad & \mathrm{per}(U) - \det(U) &= 2U_{21}U_{12}.
\end{aligned}
$$

Furthermore we want to introduce simpler expressions for the terms including the mean frequency and standard deviation:

$$
\zeta = \frac{\sigma_1\sigma_2}{\sigma_1^2+\sigma_2^2}\exp\left(-\frac{(\Omega_1-\Omega_2)^2}{2(\sigma_1^2+\sigma_2^2)}\right),\ \xi = \frac{\sigma_1^2\sigma_2^2}{\sigma_1^2+\sigma_2^2} \qquad (A.11)
$$

Inserting (A.10) and (A.11) in (A.9) we get the compact end result

$$P_{11}(\Delta\tau) = \frac{1}{2}\left(|\mathrm{per}(B)|^2 + |\det(B)|^2\right) + \zeta\left(|\mathrm{per}(B)|^2 - |\det(B)|^2\right)\mathrm{e}^{-2\xi\Delta\tau^2}. \tag{A.12}$$

In case of three photons the approach is the same as for two photons. The spectral overlap integral has the form

$$P_{111}(\Delta\tau_1, \Delta\tau_2) = \int d\omega \int d\omega' \int d\omega'' |\langle 111|U^\dagger a_1^\dagger(\omega) a_2^\dagger(\omega') a_3^\dagger(\omega'')|0\rangle|^2, \tag{A.13}$$

where $a_1^\dagger(\omega)$, $a_2^\dagger(\omega')$ and $a_3^\dagger(\omega'')$ stand for creation operators in modes $1, 2$, and 3 for photons, which all have different spectral shape functions dependent on the frequency variables $\omega, \omega', \omega''$. Since a detailed calculation for this case would be too extensive, we leave it at this point.

A.2 Three-photon coincident rate

As already mentioned in the main text, the authors of [35] show a method to derive from (2.26) to a simplified decomposition by introducing six-dimensional vectors and matrices. In this section this is will be shown in detail. Lets start with the output probability for three photons, expressed by the linear superposition

$$
\begin{aligned}
&P_{111}(\Delta\tau_1,\Delta\tau_2)=\int d\omega\int d\omega'\int d\omega''|\langle 111|\hat{R}^\dagger a_1^\dagger(\omega)a_2^\dagger(\omega')a_3^\dagger(\omega'')|0\rangle|^2\\
&=\frac{1}{6}|\mathrm{det}(R)|^2+\frac{2}{9}|\mathrm{imm}(R_{132})|^2+\frac{1}{9}\mathrm{imm}^*(R_{132})\mathrm{imm}(R_{213})+\frac{1}{9}\mathrm{imm}(R_{132})\mathrm{imm}^*(R_{213})\\
&+\frac{2}{9}|\mathrm{imm}(R_{213})|^2+\frac{2}{9}|\mathrm{imm}(R_{312})|^2+\frac{2}{9}|\mathrm{imm}(R)|^2+\frac{1}{9}\mathrm{imm}(R_{312})\mathrm{imm}^*(R)\\
&+\frac{1}{6}|\mathrm{per}(R)|^2+\frac{1}{9}\mathrm{imm}(R)\mathrm{imm}^*(R_{312})\\
&+\zeta_{13}\exp(-2\xi_{13}(\Delta\tau_1-\Delta\tau_2)^2)\Big(-\frac{1}{6}|\mathrm{det}(R)|^2-\frac{2}{9}\mathrm{imm}(R)\mathrm{imm}^*(R_{132})-\frac{1}{9}\mathrm{imm}(R)\mathrm{imm}^*(R_{213})\\
&-\frac{1}{9}\mathrm{imm}^*(R_{132})\mathrm{imm}(R_{312})+\frac{1}{9}\mathrm{imm}^*(R_{213})\mathrm{imm}(R_{312})-\frac{1}{9}\mathrm{imm}(R_{132})\mathrm{imm}^*(R_{312})\\
&+\frac{1}{9}\mathrm{imm}(R_{213})\mathrm{imm}^*(R_{312})-\frac{2}{9}\mathrm{imm}(R_{132})\mathrm{imm}^*(R)-\frac{1}{9}\mathrm{imm}(R_{213})\mathrm{imm}^*(R)+\frac{1}{6}|\mathrm{per}(R)|^2\Big)\\
&+\zeta_{12}\exp(-2\xi_{12}\Delta\tau_1^2)\Big(-\frac{1}{6}|\mathrm{det}(R)|^2+\frac{1}{9}\mathrm{imm}(R)\mathrm{imm}^*(R_{132})+\frac{2}{9}\mathrm{imm}(R)\mathrm{imm}^*(R_{213})\\
&+\frac{2}{9}\mathrm{imm}^*(R_{132})\mathrm{imm}(R_{312})+\frac{1}{9}\mathrm{imm}^*(R_{213})\mathrm{imm}(R_{312})+\frac{2}{9}\mathrm{imm}(R_{132})\mathrm{imm}^*(R_{312})\\
&+\frac{1}{9}\mathrm{imm}(R_{213})\mathrm{imm}^*(R_{312})+\frac{1}{9}\mathrm{imm}(R_{132})\mathrm{imm}^*(R)+\frac{2}{9}\mathrm{imm}(R_{213})\mathrm{imm}^*(R)+\frac{1}{6}|\mathrm{per}(R)|^2\Big)\\
&+\zeta_{23}\exp(-2\xi_{23}\Delta\tau_2^2)\Big(-\frac{1}{6}|\mathrm{det}(R)|^2+\frac{1}{9}\mathrm{imm}(R)\mathrm{imm}^*(R_{132})-\frac{1}{9}\mathrm{imm}(R)\mathrm{imm}^*(R_{213})\\
&-\frac{1}{9}\mathrm{imm}^*(R_{132})\mathrm{imm}(R_{312})-\frac{2}{9}\mathrm{imm}^*(R_{213})\mathrm{imm}(R_{312})-\frac{1}{9}\mathrm{imm}(R_{132})\mathrm{imm}^*(R_{312})\\
&-\frac{2}{9}\mathrm{imm}(R_{213})\mathrm{imm}^*(R_{312})+\frac{1}{9}\mathrm{imm}(R_{132})\mathrm{imm}^*(R)-\frac{1}{9}\mathrm{imm}(R_{213})\mathrm{imm}^*(R)+\frac{1}{6}|\mathrm{per}(R)|^2\Big)\\
&+\zeta_{123}\exp(-I_a+iI_s)\Big(\frac{1}{6}|\mathrm{det}(R)|^2-\frac{1}{9}|\mathrm{imm}(R_{132})|^2-\frac{2}{9}\mathrm{imm}^*(R_{132})\mathrm{imm}(R_{213})\\
&+\frac{1}{9}\mathrm{imm}(R_{132})\mathrm{imm}^*(R_{213})-\frac{1}{9}|\mathrm{imm}(R_{213})|^2+\frac{1}{9}\mathrm{imm}(R)\mathrm{imm}^*(R_{312})-\frac{1}{9}|\mathrm{imm}(R_{312})|^2\\
&-\frac{1}{9}|\mathrm{imm}(R)|^2-\frac{2}{9}\mathrm{imm}(R_{312})\mathrm{imm}^*(R)+\frac{1}{6}|\mathrm{per}(R)|^2\Big)\\
&+\zeta_{123}\exp(-I_a-iI_s)\Big(\frac{1}{6}|\mathrm{det}(R)|^2-\frac{1}{9}|\mathrm{imm}(R_{132})|^2-\frac{2}{9}\mathrm{imm}(R_{132})\mathrm{imm}^*(R_{213})\\
&+\frac{1}{9}\mathrm{imm}^*(R_{132})\mathrm{imm}(R_{213})-\frac{1}{9}|\mathrm{imm}(R_{213})|^2+\frac{1}{9}\mathrm{imm}^*(R)\mathrm{imm}(R_{312})-\frac{1}{9}|\mathrm{imm}(R_{312})|^2\\
&-\frac{1}{9}|\mathrm{imm}(R)|^2-\frac{2}{9}\mathrm{imm}^*(R_{312})\mathrm{imm}(R)+\frac{1}{6}|\mathrm{per}(R)|^2\Big)\ ,
\end{aligned}
$$

with

$$
\begin{aligned}
\zeta_{123} =&\sqrt{\zeta_{12}\zeta_{23}\zeta_{13}},\\
I_a \equiv&I_a(\Delta\tau_1,\Delta\tau_2) = -(\Delta\tau_1)^2\xi_{12} - (\Delta\tau_1-\Delta\tau_2)^2\xi_{13} - (\Delta\tau_2)^2\xi_{23},\\
I_s \equiv&I_s(\Delta\tau_1,\Delta\tau_2) = \Delta\tau_1\nu_{12} + (\Delta\tau_1-\Delta\tau_2)\nu_{13} - \Delta\tau_2\nu_{23},\\
\zeta_{ij} =&\frac{2\sigma_i\sigma_j}{\sigma_i^2+\sigma_j^2}\exp\left(-\frac{(\omega_{c,i}-\omega_{c,j})^2}{2(\sigma_i^2+\sigma_j^2)}\right), && \text{(A.14)}\\
\xi_{ij} =&\frac{2\sigma_i^2\sigma_j^2}{\sigma_i^2+\sigma_j^2},\ \nu_{ij} = \frac{\omega_{c,i}\sigma_j^2+\omega_{c,j}\sigma_i^2}{\sigma_i^2+\sigma_j^2}. && \text{(A.15)}
\end{aligned}
$$

The modes are labeled $1\to i$, $2\to j$, and $3\to k$, so R_{ijk} is the matrix R with permuting rows. By introducing six matrices $\mathbb{1}$, ρ_{12}, ρ_{13}, ρ_{23}, ρ_{123}, and ρ_{132} the 60 terms expression can be simplified to

$$
\begin{aligned}
P_{111}(\Delta\tau_1,\Delta\tau_2) = \boldsymbol{v}^\dagger\big(&\mathbb{1} + \rho_{12}\zeta_{12}e^{-\xi_{12}\Delta\tau_1^2} + \rho_{23}\zeta_{23}e^{-\xi_{23}\Delta\tau_2^2}\\
&+ \rho_{13}\zeta_{13}e^{-\xi_{13}(\Delta\tau_1-\Delta\tau_2)^2} + \zeta_{123}\big(\rho_{123}\mathrm{e}^{\xi_{123}(\Delta\tau_1,\Delta\tau_2)} + \rho_{132}\mathrm{e}^{\xi_{123}^*(\Delta\tau_1,\Delta\tau_2)}\big)\big)\boldsymbol{v}\ , \quad \text{(A.16)}
\end{aligned}
$$

where

$$\xi_{123}(\Delta\tau_1,\Delta\tau_2) = I_a + iI_s. \tag{A.17}$$

This expression gets its compact form due to introducing of six-dimensional vectors. The vector $\boldsymbol{v}$ contains all contributions of immanants, determinant and permanent of the submatrix R and the subscripts specify the input modes of the photons.

$$
\boldsymbol{v} \equiv \begin{pmatrix}
\mathrm{per}(R)\\
\det(R)\\
\frac{1}{2\sqrt{3}}\mathrm{imm}(R) + \frac{1}{2\sqrt{3}}\mathrm{imm}(R_{213})\\
\frac{1}{6}\mathrm{imm}(R) - \frac{1}{3}\mathrm{imm}(R_{132}) - \frac{1}{6}\mathrm{imm}(R_{213}) + \frac{1}{3}\mathrm{imm}(R_{312})\\
\frac{1}{6}\mathrm{imm}(R) + \frac{1}{3}\mathrm{imm}(R_{132}) + \frac{1}{6}\mathrm{imm}(R_{213}) + \frac{1}{3}\mathrm{imm}(R_{312})\\
-\frac{1}{2\sqrt{3}}\mathrm{imm}(R) + \frac{1}{2\sqrt{3}}\mathrm{imm}(R_{213})
\end{pmatrix}. \tag{A.18}
$$

ϱ_{12},ϱ_{13},ϱ_{23} and ϱ_{123} are permutation matrices describing the symmetry under exchange of the photons. They are reduced to a block-diagonal form via a change of basis. Now the new basis vectors are components of the vector $\boldsymbol{v}$ above.

$$\mathbb{1} = \begin{pmatrix} 1 & 0 & 0 & 0 & 0 & 0 \\ 0 & 1 & 0 & 0 & 0 & 0 \\ 0 & 0 & 1 & 0 & 0 & 0 \\ 0 & 0 & 0 & 1 & 0 & 0 \\ 0 & 0 & 0 & 0 & 1 & 0 \\ 0 & 0 & 0 & 0 & 0 & 1 \end{pmatrix}, \rho_{12} = \begin{pmatrix} 1 & 0 & 0 & 0 & 0 & 0 \\ 0 & -1 & 0 & 0 & 0 & 0 \\ 0 & 0 & 1 & 0 & 0 & 0 \\ 0 & 0 & 0 & -1 & 0 & 0 \\ 0 & 0 & 0 & 0 & 1 & 0 \\ 0 & 0 & 0 & 0 & 0 & -1 \end{pmatrix},$$

$$\rho_{23} = \begin{pmatrix} 1 & 0 & 0 & 0 & 0 & 0 \\ 0 & -1 & 0 & 0 & 0 & 0 \\ 0 & 0 & -\frac{1}{2} & -\frac{\sqrt{3}}{2} & 0 & 0 \\ 0 & 0 & -\frac{\sqrt{3}}{2} & \frac{1}{2} & 0 & 0 \\ 0 & 0 & 0 & 0 & -\frac{1}{2} & -\frac{\sqrt{3}}{2} \\ 0 & 0 & 0 & 0 & -\frac{\sqrt{3}}{2} & \frac{1}{2} \end{pmatrix}, \rho_{13} = \begin{pmatrix} 1 & 0 & 0 & 0 & 0 & 0 \\ 0 & -1 & 0 & 0 & 0 & 0 \\ 0 & 0 & -\frac{1}{2} & \frac{\sqrt{3}}{2} & 0 & 0 \\ 0 & 0 & \frac{\sqrt{3}}{2} & \frac{1}{2} & 0 & 0 \\ 0 & 0 & 0 & 0 & -\frac{1}{2} & \frac{\sqrt{3}}{2} \\ 0 & 0 & 0 & 0 & \frac{\sqrt{3}}{2} & \frac{1}{2} \end{pmatrix},$$

$$\rho_{123} = \begin{pmatrix} 1 & 0 & 0 & 0 & 0 & 0 \\ 0 & 1 & 0 & 0 & 0 & 0 \\ 0 & 0 & -\frac{1}{2} & -\frac{\sqrt{3}}{2} & 0 & 0 \\ 0 & 0 & \frac{\sqrt{3}}{2} & -\frac{1}{2} & 0 & 0 \\ 0 & 0 & 0 & 0 & -\frac{1}{2} & -\frac{\sqrt{3}}{2} \\ 0 & 0 & 0 & 0 & \frac{\sqrt{3}}{2} & -\frac{1}{2} \end{pmatrix}, \rho_{132} = \begin{pmatrix} 1 & 0 & 0 & 0 & 0 & 0 \\ 0 & 1 & 0 & 0 & 0 & 0 \\ 0 & 0 & -\frac{1}{2} & \frac{\sqrt{3}}{2} & 0 & 0 \\ 0 & 0 & -\frac{\sqrt{3}}{2} & -\frac{1}{2} & 0 & 0 \\ 0 & 0 & 0 & 0 & -\frac{1}{2} & \frac{\sqrt{3}}{2} \\ 0 & 0 & 0 & 0 & -\frac{\sqrt{3}}{2} & -\frac{1}{2} \end{pmatrix}. \tag{A.19}$$

All the information about the physical properties of the interfering photons are contained in the ζ terms and ξ terms, whereas the effect of the permutation symmetry is expressed in the vector $\boldsymbol{v}$ and the permutation matrices ρ.

Appendix B

Experimental Data

B.1 Spectral Shape of the Photons

Here the spectral shape of all three photons, used for the experiment "Boson Sampling with Controllable Distinguishability" is shown.

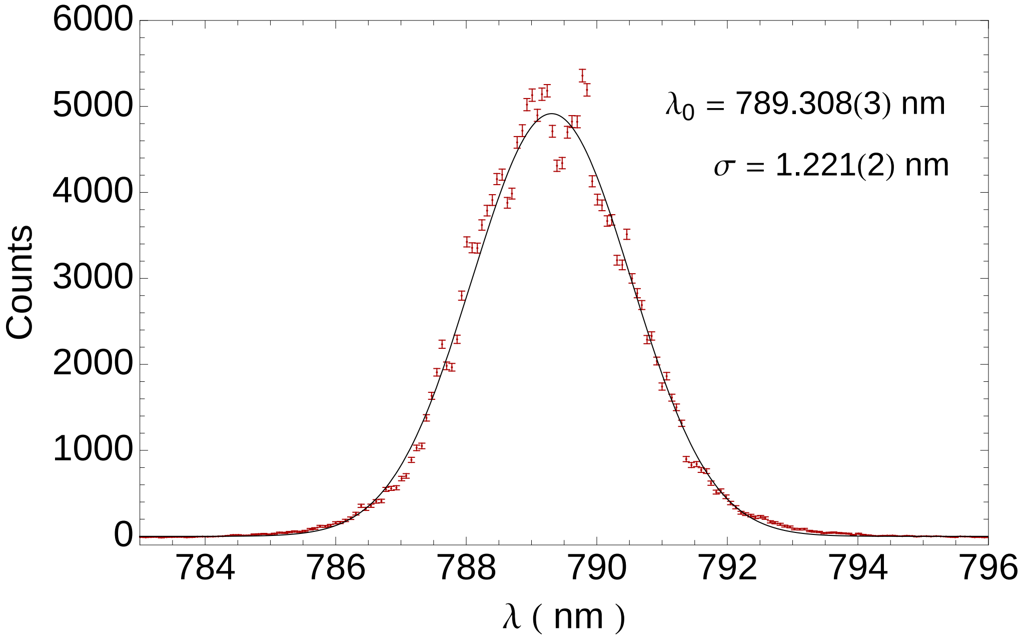

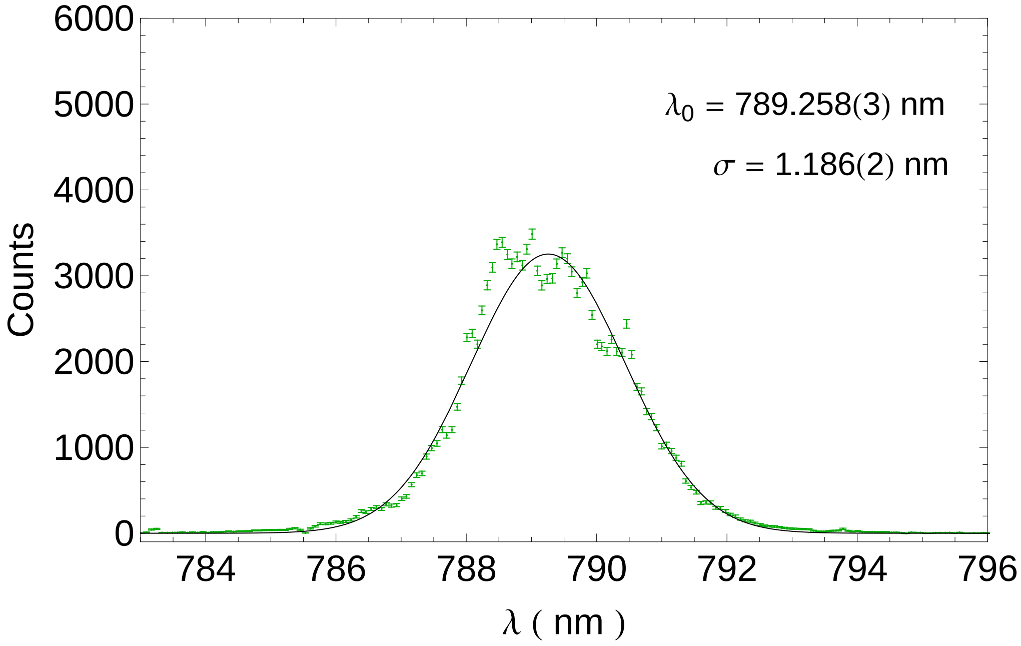
6000
5000
4000
3000
2000
1000
0
Counts
784
786
788
790
792
794
796
λ (nm)
λ_0 = 789.258(3) nm
σ = 1.186(2) nm

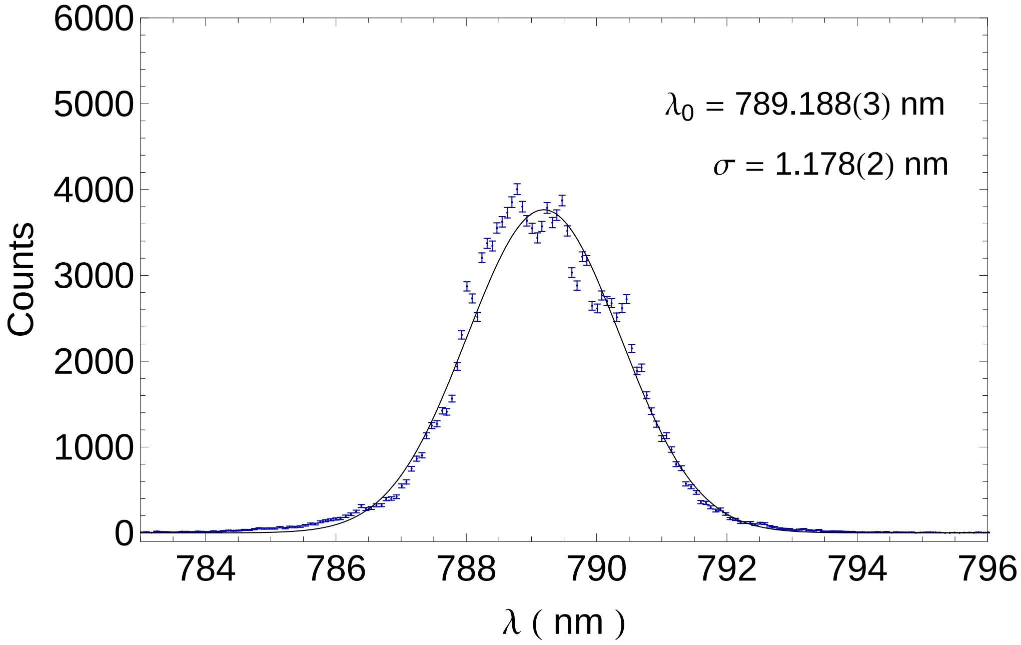
6000
5000
4000
3000
2000
1000
0
Counts
784
786
788
790
792
794
796
λ (nm)
λ_0 = 789.188(3) nm
σ = 1.178(2) nm

B.2 Recorded Data for In124

In the following tables the mean value of the coincidence counts, their standard deviation and the theoretical predicted values are shown.

Recorded Coincidence Counts - Mean						
out	Point 1	Point 2	Point 3	Point 4	Point 5	Point 6
124	11.000	9.578	11.632	12.368	11.316	11.474
134	84.474	58.368	80.842	79.579	67.053	72.368
345	385.895	627.789	500.789	628.211	554.105	798.737
123	4.105	6.5263	8.263	11.263	6.737	9.000
234	58.316	53.368	57.947	60.526	59.632	56.053
235	62.737	82.737	57.421	54.474	59.526	63.053
145	64.632	124.789	77.842	94.842	81.895	99.579
125	12.211	11.000	16.053	16.105	16.737	16.368
135	64.526	88.316	83.000	113.421	152.789	135.316
245	68.158	77.211	79.421	87.421	67.895	95.842

Table B.1: Mean value of the recorded coincidence counts for the 10 possible output combinations.

Recorded Coincidence Counts - Standard Deviation						
out	Point 1	Point 2	Point 3	Point 4	Point 5	Point 6
124	1.035	0.965	0.509	0.915	1.254	0.893
134	4.013	3.076	4.778	4.416	3.324	3.617
345	20.699	30.311	26.493	31.462	23.926	31.283
123	0.567	0.668	0.791	0.820	0.625	0.749
234	3.108	2.509	3.190	3.178	3.166	2.681
235	3.237	4.713	3.277	3.382	3.102	3.309
145	3.722	6.271	3.923	5.385	4.314	4.0949
125	0.993	0.738	1.025	1.121	1.157	1.443
135	3.420	4.475	4.108	5.188	6.908	5.849
245	3.348	4.774	4.528	5.337	3.505	3.835

Table B.2: Standard deviation of the recorded coincidence counts for the 10 possible output combinations.

B.3 Data for Plots

Normalized Mean						
out	Point 1	Point 2	Point 3	Point 4	Point 5	Point 6
124	0.0134795	0.0084049	0.0119518	0.0106789	0.0105001	0.0084503
134	0.1035150	0.0512146	0.0830674	0.0687085	0.0622192	0.0532987
345	0.4728800	0.5508450	0.5145750	0.5423980	0.5141630	0.5882630
123	0.0050306	0.0057264	0.0084906	0.0097246	0.0062512	0.0066284
234	0.0714608	0.0468274	0.0595425	0.0522585	0.0553331	0.0412823
235	0.0768784	0.0725963	0.0590017	0.0470326	0.0552354	0.0464377
145	0.0792003	0.1094950	0.0799849	0.0818868	0.0759914	0.0733390
125	0.0149629	0.0096518	0.0164945	0.0139053	0.0155304	0.0120552
135	0.0790713	0.0774915	0.0852847	0.0979278	0.1417760	0.0996589
245	0.0835214	0.0677473	0.0816073	0.0754794	0.0630006	0.0705869

Normalized Standard Deviation						
out	Point 1	Point 2	Point 3	Point 4	Point 5	Point 6
124	0.0012677	0.0008469	0.0005225	0.0007901	0.0011639	0.0006577
134	0.0049172	0.0026992	0.0049098	0.0038126	0.0030845	0.0026639
345	0.0253648	0.0265957	0.0272224	0.0271650	0.0222016	0.0230398
123	0.0006943	0.0005864	0.0008122	0.0007076	0.0005801	0.0005518
234	0.0038089	0.0022012	0.0032772	0.0027441	0.0029379	0.0019748
235	0.0039668	0.0041351	0.0033672	0.0029196	0.0028783	0.0024371
145	0.0045603	0.0055028	0.0040314	0.0046492	0.0040033	0.0030158
125	0.0012167	0.0006471	0.0010527	0.0009679	0.0010734	0.0010630
135	0.0041902	0.0039263	0.0042205	0.0044792	0.0064098	0.0043077
245	0.0041022	0.0041890	0.0046529	0.0046078	0.0032525	0.0028241

Normalized Theory Values						
out	Point 1	Point 2	Point 3	Point 4	Point 5	Point 6
124	0.0168806	0.0083511	0.0151860	0.0115396	0.0106878	0.0082613
134	0.1103760	0.0435907	0.0868893	0.0641839	0.0540391	0.0510700
345	0.4594640	0.5461870	0.4897530	0.5464730	0.5197250	0.5876640
123	0.0017077	0.0053614	0.0067422	0.0099967	0.0053660	0.0067762
234	0.0753403	0.0488730	0.0651696	0.0518716	0.0546698	0.0400620
235	0.0768054	0.0739559	0.0471422	0.0373823	0.0409616	0.0350419
145	0.0864042	0.1253520	0.0673241	0.0766483	0.0716931	0.0725172
125	0.0147081	0.0090362	0.0188133	0.0162785	0.0186653	0.0141971
135	0.0582768	0.0619696	0.1113560	0.0983153	0.1484650	0.1028110
245	0.1000380	0.0773228	0.0916235	0.0873105	0.0757273	0.0815990

Bibliography

[1] Richard P Feynman. Simulating physics with computers. *International journal of theoretical physics*, 21(6):467–488, 1982.

[2] Alan M Turing. Intelligent machinery, a heretical theory. *The Turing Test: Verbal Behavior as the Hallmark of Intelligence*, page 105, 1948.

[3] David Deutsch. Quantum theory, the church-turing principle and the universal quantum computer. *Proceedings of the Royal Society of London. A. Mathematical and Physical Sciences*, 400(1818):97–117, 1985.

[4] Peter W Shor. Algorithms for quantum computation: discrete logarithms and factoring. In *Foundations of Computer Science, 1994 Proceedings., 35th Annual Symposium on*, pages 124–134. IEEE, 1994.

[5] Lov K Grover. Quantum mechanics helps in searching for a needle in a haystack. *Physical review letters*, 79(2):325, 1997.

[6] Adriano Barenco, Charles H Bennett, Richard Cleve, David P DiVincenzo, Norman Margolus, Peter Shor, Tycho Sleator, John A Smolin, and Harald Weinfurter. Elementary gates for quantum computation. *Physical Review A*, 52(5):3457, 1995.

[7] Michael A Nielsen and Isaac L Chuang. *Quantum computation and quantum information.* Cambridge university press, 2010.

[8] Emanuel Knill, Raymond Laflamme, and Gerald J Milburn. A scheme for efficient quantum computation with linear optics. *nature*, 409(6816):46–52, 2001.

[9] Sara Gasparoni, Jian-Wei Pan, Philip Walther, Terry Rudolph, and Anton Zeilinger. Realization of a photonic controlled-not gate sufficient for quantum computation. *Physical review letters*, 93(2):020504, 2004.

[10] Wei-Bo Gao, Alexander M Goebel, Chao-Yang Lu, Han-Ning Dai, Claudia Wagenknecht, Qiang Zhang, Bo Zhao, Cheng-Zhi Peng, Zeng-Bing Chen, Yu-Ao Chen, et al. Teleportation-based realization of an optical quantum two-qubit entangling gate. *Proceedings of the National Academy of Sciences*, 107(49):20869–20874, 2010.

[11] Emanuel Knill and Raymond Laflamme. Power of one bit of quantum information. *Physical Review Letters*, 81(25):5672, 1998.

[12] Scott Aaronson and Daniel Gottesman. Improved simulation of stabilizer circuits. *Physical Review A*, 70(5):052328, 2004.

[13] Stephen P Jordan. Permutational quantum computing. *arXiv preprint arXiv:0906.2508*, 2009.

[14] Scott Aaronson and Alex Arkhipov. The computational complexity of linear optics. In *Proceedings of the 43rd annual ACM symposium on Theory of computing*, pages 333–342. ACM, 2011.

[15] David P Divincenzo. The physical implementation of quantum computation. *Fortschritte der Physik*, 48:771–783, 2000.

[16] R. Raussendorf and H. J. Briegel. A one-way quantum computer. *Physical Review Letters Lett.* ,, 86(4):5188–5191, 2001.

[17] NJ Cerf, C Adami, and PG Kwiat. Optical simulation of quantum logic. *Physical Review A*, 57(3):R1477, 1998.

[18] Pieter Kok, William J Munro, Kae Nemoto, Timothy C Ralph, Jonathan P Dowling, and GJ Milburn. Linear optical quantum computing with photonic qubits. *Reviews of Modern Physics*, 79(1):135, 2007.

[19] Daniel Gottesman and Isaac L Chuang. Demonstrating the viability of universal quantum computation using teleportation and single-qubit operations. *Nature*, 402(6760):390–393, 1999.

[20] Y. Aharonov, L. Davidovich, and N. Zagury. Quantum random walks. *Phys. Rev. A*, 48:1687–1690, Aug 1993. doi: 10.1103/PhysRevA.48.1687. URL `http://link.aps.org/doi/10.1103/PhysRevA.48.1687`.

[21] Max Born. The statistical interpretation of quantum mechanics. *Nobel Lecture*, 11:1942–1962, 1954.

[22] Alex Arkhipov and Greg Kuperberg. The bosonic birthday paradox. *arXiv preprint arXiv:1106.0849*, 2011.

[23] Matthew A Broome, Alessandro Fedrizzi, Saleh Rahimi-Keshari, Justin Dove, Scott Aaronson, Timothy C Ralph, and Andrew G White. Photonic boson sampling in a tunable circuit. *Science*, 339(6121):794–798, 2013.

[24] Justin B Spring, Benjamin J Metcalf, Peter C Humphreys, W Steven Kolthammer, Xian-Min Jin, Marco Barbieri, Animesh Datta, Nicholas Thomas-Peter, Nathan K Langford, Dmytro Kundys, et al. Boson sampling on a photonic chip. *Science*, 339(6121):798–801, 2013.

[25] Max Tillmann, Borivoje Dakić, René Heilmann, Stefan Nolte, Alexander Szameit, and Philip Walther. Experimental boson sampling. *Nature Photonics*, 2013.

[26] Andrea Crespi, Roberto Osellame, Roberta Ramponi, Daniel J Brod, Ernesto F Galvão, Nicolò Spagnolo, Chiara Vitelli, Enrico Maiorino, Paolo Mataloni, and Fabio Sciarrino. Integrated multimode interferometers with arbitrary designs for photonic boson sampling. *Nature Photonics*, 2013.

[27] Thomas Young. The bakerian lecture: On the theory of light and colours. *Philosophical Transactions of the Royal Society of London*, 92:pp. 12–48, 1802. ISSN 02610523. URL `http://www.jstor.org/stable/107113`.

[28] Richard P Feynman, Robert B Leighton, and Matthew Sands. Lectures on physics, vol. iii, 1965.

[29] Leon M Lederman and Christopher T Hill. *Quantum physics for poets*. PrometheusBooks, 2011.

[30] C. K. Hong, Z. Y. Ou, and L. Mandel. Measurement of subpicosecond time intervals between two photons by interference. *Phys. Rev. Lett.*, 59: 2044–2046, Nov 1987. doi: 10.1103/PhysRevLett.59.2044. URL http://link.aps.org/doi/10.1103/PhysRevLett.59.2044.

[31] H. Fearn and R. Loudon. Theory of two-photon interference. *J. Opt. Soc. Am. B*, 6(5):917–927, May 1989. doi: 10.1364/JOSAB.6.000917. URL http://josab.osa.org/abstract.cfm?URI=josab-6-5-917.

[32] Pieter Kok and Brendon W Lovett. *Introduction to optical quantum information processing*. Cambridge University Press, 2010.

[33] Si-Hui Tan, Yvonne Y. Gao, Hubert de Guise, and Barry C. Sanders. Su(3) quantum interferometry with single-photon input pulses. *Phys. Rev. Lett.*, 110:113603, Mar 2013. doi: 10.1103/PhysRevLett.110.113603. URL http://link.aps.org/doi/10.1103/PhysRevLett.110.113603.

[34] Hubert de Guise, Si-Hui Tan, Isaac P Poulin, and Barry C Sanders. Immanants for three-channel linear optical networks. *arXiv preprint arXiv:1402.2391*, 2014.

[35] Max Tillmann, Si-Hui Tan, Sarah E Stoeckl, Barry C Sanders, Hubert de Guise, René Heilmann, Stefan Nolte, Alexander Szameit, and Philip Walther. Bosonsampling with controllable distinguishability. *arXiv preprint arXiv:1403.3433*, 2014.

[36] S Ramelow, A Mech, M Giustina, S Gröblacher, W Wieczorek, J Beyer, A Lita, B Calkins, T Gerrits, SW Nam, et al. Highly efficient heralding of entangled single photons. *Optics express*, 21(6):6707–6717, 2013.

[37] MD Eisaman, J Fan, A Migdall, and SV Polyakov. Invited review article: Single-photon sources and detectors. *Review of Scientific Instruments*, 82 (7):071101–071101, 2011.

[38] A Saleh BE and MC Teich. Fundamentals of photonics, 1991.

[39] Eugene Hecht and A Zajac. Optics, ed. *MA: Addison-Wesley Publishing Company*, 1998.

[40] Kazuyoshi Itoh, Wataru Watanabe, Stefan Nolte, and Chris B Schaffer. Ultrafast processes for bulk modification of transparent materials. *MRS bulletin*, 31(08):620–625, 2006.

[41] John Robert Taylor. *An introduction to error analysis: the study of uncertainties in physical measurements.* University science books, 1997.

[42] Anthony Laing and Jeremy L O'Brien. Super-stable tomography of any linear optical device. *arXiv preprint arXiv:1208.2868*, 2012.

Curriculum Vitea

Personal Data

NAME:	Sarah Stöckl
DATE OF BIRTH:	19 March 1987
PLACE OF BIRTH:	Zams, Austria
CITIZENSHIP:	Austrian
LANGUAGES:	German, English, French

Education

OCT 2012 - CURRENT	**MSc Physics** University of Vienna
OCT 2010 - SEP 2012	**BSc Physics** University of Vienna
OCT 2007 - SEP 2011	**BSc Astronomy** University of Vienna
OCT 2005 - OCT 2010	**BA Theater, Film and Media** University of Vienna
SEP 2001 - JUN 2005	**Secondary School** KORG Zams

Vienna, Oct 2014